JGR Planets

REVIEW ARTICLE

10.1029/2023JE008248

Key Points:

- Capillarity is involved in numberless natural processes
- During past decades, the presence of liquid phase of different nature has been detected on several extraterrestrial bodies of the solar system
- We review and discuss physical processes that may have important consequences in planetary science like the transport of organic material between planetary interior and the atmosphere

Correspondence to:

D. Cordier,
daniel.cordier@univ-reims.fr

Citation:

Cordier, D., Liger-Belair, G., Bonhommeau, D. A., Séon, T., Appéré, T., & Carrasco, N. (2024). Capillary processes in extraterrestrial contexts. *Journal of Geophysical Research: Planets*, *129*, e2023JE008248. https://doi.org/10.1029/2023JE008248

Received 15 DEC 2023
Accepted 12 APR 2024

Author Contributions:

Conceptualization: Daniel Cordier, Gérard Liger-Belair, Nathalie Carrasco
Investigation: Daniel Cordier, Gérard Liger-Belair, Nathalie Carrasco
Methodology: Daniel Cordier, Gérard Liger-Belair, David A. Bonhommeau, Thomas Séon, Nathalie Carrasco
Software: Daniel Cordier
Validation: Daniel Cordier
Writing – original draft: Daniel Cordier, Thomas Appéré

Capillary Processes in Extraterrestrial Contexts

Daniel Cordier[1], Gérard Liger-Belair[1], David A. Bonhommeau[2], Thomas Séon[3], Thomas Appéré[4], and Nathalie Carrasco[5]

[1]CNRS, GSMA, UMR 7331, Université de Reims Champagne Ardenne, Reims, France, [2]CNRS, LAMBE, Université Paris-Saclay, Université Evry, CY Cergy Paris Université, Evry-Courcouronnes, France, [3]CNRS, UMR 7190, Institut Jean Le Rond d'Alembert, Sorbonne Université, Paris, France, [4]Lycée Saint-Paul, Vannes, France, [5]LATMOS, UMR CNRS 8190, Université Versailles St Quentin, UPMC Université Paris 06, Guyancourt, France

Abstract The Earth is no longer the only known celestial body containing one or more liquid phases. The Cassini spacecraft has discovered seas of hydrocarbons at the surface of Titan, while a series of corroborating evidences argue in favor of the existence of an aqueous ocean beneath the icy crust of several moons. Capillarity embraces a family of physical processes occurring at the free surface of a liquid. These phenomena depend on the liquid properties and on the local planetary conditions. Capillarity may have important direct or indirect implications on the geoscientific and astrobiological points of view. In this paper, we discuss capillarity physics among solar system objects and expected consequences for planetary science.

Plain Language Summary The formation of raindrops, the production of tiny liquid droplets by bubble bursting at the surface of an ocean, or even the floatation of small solid particles at this surface, are examples of capillarity effects, physical processes which can be observed in everyday life. In this work, we discuss such phenomena in extraterrestrial contexts where large amount of liquids have be detected during past decades by space exploration.

1. Introduction

In everyday life, capillary action manifests itself in many different ways, going from liquid ascension in fibers to the dynamics of bubbles and droplets. On a scientific point of view, hydrodynamics of capillarity is a rather old field, but it is still the subject of very active researches (de Gennes et al., 2004; Drelich et al., 2020) with a wide variety of applications like the manufacture of micro-lenses or the understanding of blood circulation. In all these physical processes, we always find at least one interface between two immiscible liquids, or a liquid and a vapor. We also have situations involving three phases: two liquids and a solid; this is the case in problems related to surface wetting. These interfaces have particular hydrodynamic behaviors, this specificity is fundamentally governed by different states of molecules in the vicinity of the interface (see Figure 1) compared to molecules in the midst of the liquid (de Gennes et al., 2004). As shown in Figure 1, this dichotomy is explained by the loss of half of cohesive interactions by molecules located at the surface.

In this work, we investigate the role of capillarity in some phenomena relevant to planetary contexts. The two last decades of space exploration have revealed the existence of several extraterrestrial liquid phases: liquid methane-ethane-nitrogen mixtures in Titan's polar regions (Stofan et al., 2007), liquid water for Enceladus (Porco et al., 2006) and probably Europa (Roth, 2021; Roth et al., 2014; Sparks et al., 2017), while many evidence speak in favor of the massive presence of liquid water at the surface of Mars, 3 to 4 billions years ago (Nazari-Sharabian et al., 2020).

In order to compare the relative importance of capillarity and gravity, physicists have introduced the Bond number *Bo* (also called Eötvös number) (Séon, 2018)

$$Bo = \frac{\rho_{\mathrm{liq}} g L^2}{\sigma} \tag{1}$$

with ρ_{liq} the density of the liquid (kg m^{-3}), g the gravity (m s^{-2}), L the typical size (m) of a considered object, and σ the surface tension (N m^{-1}). A large Bond number, that is, $Bo \gg 1$, is the signature of a physical process where gravity has a dominant role; in the opposite situation capillarity is prominent. Clearly, for the same liquid at the surface of celestial bodies where gravity is smaller than the terrestrial one, the effects of capillarity may be

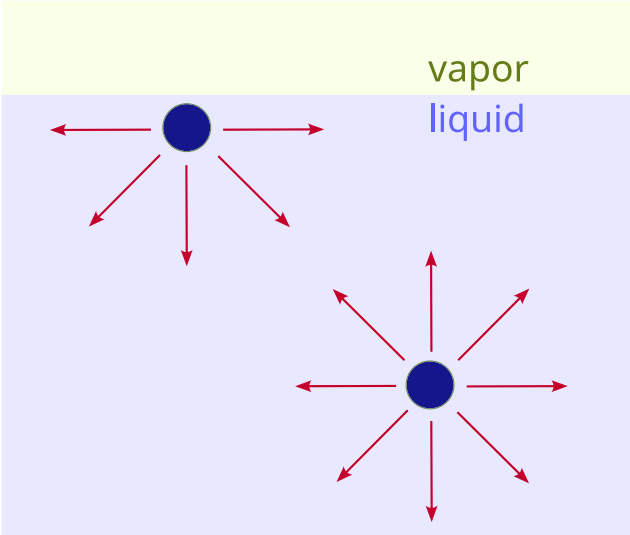

Figure 1. A schematic view of a liquid-vapor interface, two "molecules" are represented by blue circles, while the intermolecular interactions are symbolized by red arrows.

significantly reinforced. If we consider the capillary length $l_c = \sqrt{\sigma/\rho g}$ (cf., p. 33 de Gennes et al. (2004)), we see that effects of capillarity should be important for larger objects under lower gravity. For instance, the small kronian satellite, Enceladus, has a crust dotted by cracks (Postberg et al., 2018), where the presence of liquid water is suspected. The influence of capillarity should be strong there, compared with what we have at the surface of the Earth, since the gravity of Enceladus is around 0.11 m s^{-2}, almost two orders of magnitude lower than the terrestrial value (9.81 m s^{-2}). By analogy with Reynolds number, we can also define the Laplace number $La = \rho\sigma L/\eta^2$ (where η is the dynamic viscosity) which quantifies the ratio between the inertio-capillary effect and viscous effects (Deike et al., 2018). In Figure 2 we have reported the behavior of *Bo* versus *La* for different planetary objects. Bodies where liquid water exists, are aligned at $La \simeq 0.3 \times 10^6$ and Titan, harboring liquid methane, stands clearly apart. This figure shows that Enceladus and Titan should exhibit the most striking differences with the Earth.

Our perspective is different from the one adopted in studies based on experiments performed under microgravity conditions (i.e., aboard the International Space Station, Weislogel et al. (2009)). In the latter case, the purpose is focused on the fundamental properties of capillary hydrodynamics, while we are discussing applications in the particular field of planetology.

In the following, we first address the problem of small solid particles floatation at the surface of a liquid, and we discuss the aerosol formation via bubble bursting through these surfaces. After these aspects focused on liquid/gas interface dynamics, we turn our attention to raindrop size distribution and expected consequences in extraterrestrial contexts. A particular focus is on possible observations by *Dragonfly*, the future space mission to Titan, that is planned to explore the surface of this satellite of Saturn by the mid-2030s.

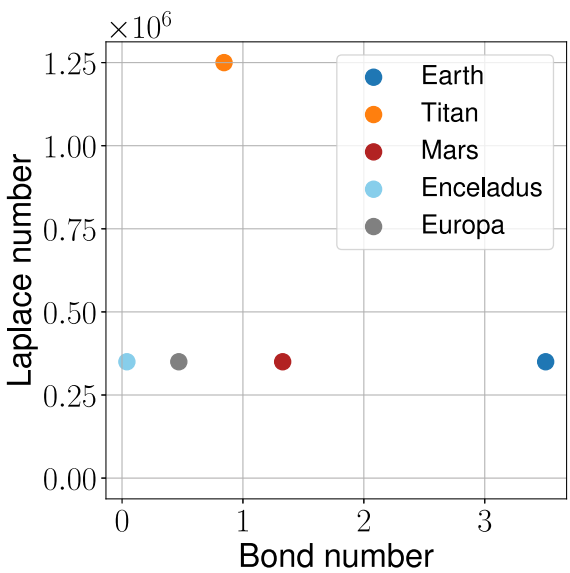

Figure 2. The Laplace number as a function of the Bond number for the planetary bodies considered in this article. The considered characteristic length *L*, required in both *La* and *Bo* computations, is the same for all bodies, and arbitrary fixed to 5 mm.

2. Floatability by Capillarity

The presence of some floating material, over an interface between a liquid phase and a gaseous phase, can lead to major consequences by affecting exchanges of energy, momentum and matter between the phases. The form of this floating material may vary from a tiny monomolecular microlayer to a thick layer similar to ice pack. At the surface of terrestrial oceans, the presence of a thin floating film, produced by biological activity (Lin et al., 2003), has a damping effect on wave activity; marine films is an important topic, and constitutes a full-fledged academic discipline (Gade et al., 2006). Broadly speaking, a solid material is able to float at a liquid surface with the help of two physical processes: (a) the well known Archimede's buoyancy force, for materials less dense than the liquid, (b) capillary forces resulting from interaction at molecular scale. This is the second effect we are studying in this paragraph.

The floatability generated by capillarity has been studied for a long time since it is essential for industrial applications based on floatation (Chipfunhu et al., 2011; Kyzas & Matis, 2018; Mousumi & Venugopal, 2016). For the sake of simplicity, classical studies of solid particles floatability consider idealized spherical particles (Crawford & Ralston, 1988; Scheludko et al., 1976) and we maintain this approach here (see Figure A1 in Appendix A). The differential equation provided by first principles can be solved numerically (see Appendix A), the main input parameters being the particle radius *R*, the planetary gravity *g*, the liquid surface tension σ, the liquid-solid contact angle θ_c, and the respective densities of the liquid (ρ_{liq}) and solid

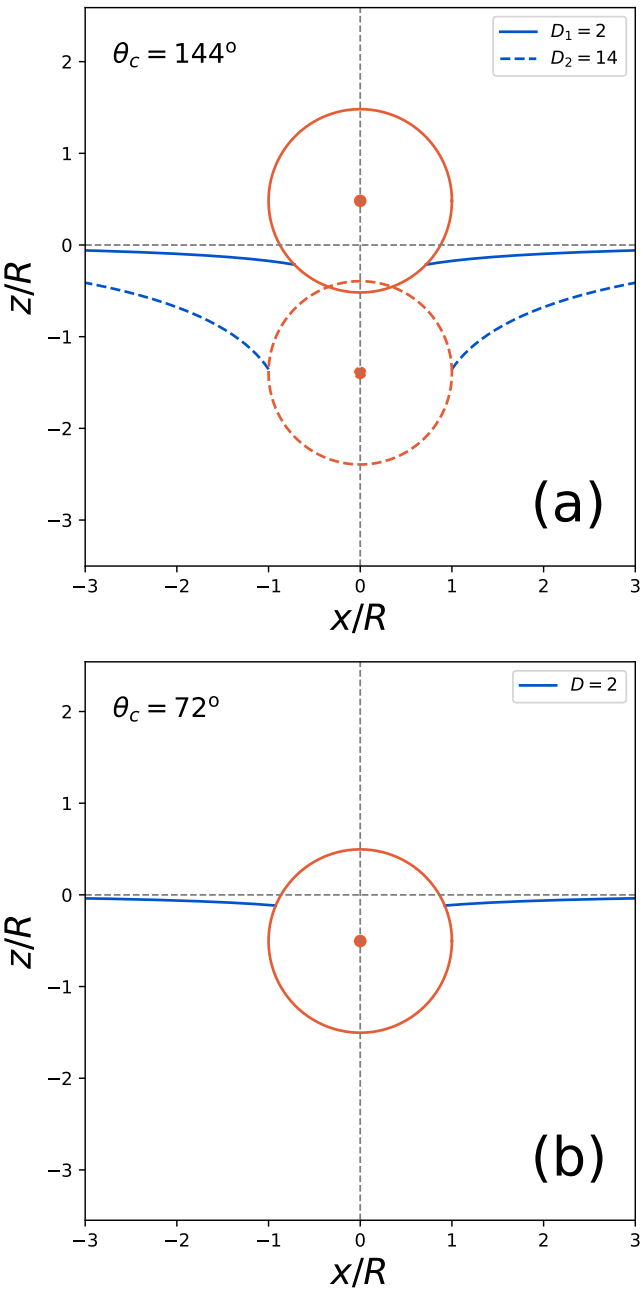

Figure 3. Meniscus profiles (in blue) due to a solid spherical particle (in orange) obtained numerically using the method described by Lee (2018). The coordinates z and x have been normalized using the particle radius R. All solutions have the same Bond number $\mathcal{B}o = 0.1$ (defined by Equation 1). (a) The influence of the density ratio $D = (\rho_{sol} - \rho_{air})/(\rho_{liq} - \rho_{air})$, for a contact angle θ_c fixed to 144°. (b) An example of flotation of a liquidophobic sphere with $\theta_c = 72°$, this result corresponds to $D = 2$.

(ρ_{sol}). Examples of results as a function of the meta-parameter $D = (\rho_{sol} - \rho_{air})/(\rho_{liq} - \rho_{air})$ can be seen in Figure 3. As expected, denser solids lead to the most incurved menisci. The liquid surface tension has the opposite effect, with almost flat liquid-air interface for high surface tension values. In Figure 3b the effect of a relatively small contact angle θ_c is represented. This case shows clearly the possibility for floatation, even in the case of liquidophobic (i.e., $\theta_c < 90°$) solid material. However, in such a situation, the filling angle θ_f (see Figure A1 in Appendix A) tends to be small. It can be easily shown that (see Appendix A) that the radius of a floating spherical particle has a maximum radius R_{max}

$$R_{max} \sim \sqrt{\frac{3\sigma}{2(\rho_{sol} - \rho_{liq})\, g}} \sin\frac{\theta_c}{2} \tag{2}$$

This equation can be found in the literature in a simplified form (see Equation 4.5 in Scheludko et al. (1976)). Not surprisingly, when ρ_{liq} tends to ρ_{sol} the radius R_{max} becomes arbitrarily large. Thus, in principle, any small enough spherical particle can float for a non-zero contact angle with the constraint $\theta_f \lesssim \theta_c$. The latter condition puts restrictions on the size of actual particles that are able to float. Up to this point, we have only considered spherical particles but the reality may be more complex. In Figure 4 we have represented examples of shapes that could favor floatability for materials with a small contact angle.

Another aspect, ignored in the above lines, concerns the stability of the equilibrium involved in flotation (Huh & Mason, 1974): is this equilibrium stable against translational or rotational perturbations? Such a question remains very complicated to answer and is clearly beyond the scope of this paper. Nonetheless, we emphasize that stability becomes an important issue when perturbations length scale, or "wavelength" if appropriate, is comparable to, or smaller than, the size of the particle to efficiently affect the stability of the system. If the perturbation is a wave, the frequency ν depends on the wavelength λ according to the dispersion relation for capillary waves (Melville, 2001)

$$\nu = \sqrt{\frac{2\pi\sigma}{\rho\lambda^3}} \tag{3}$$

In conclusion, this discussion shows us that a large category of particles can float over a liquid-gas interface, even liquidophobic materials under some conditions concerning their shape, size and contact angle.

2.1. The Case of Titan

The Cassini orbiter has revealed a collection of seas and lakes in the polar regions of Titan (see Figure 5), the largest satellite of Saturn (Stofan et al., 2007). Besides, Titan is also the only moon of the solar system possessing a dense atmosphere, which harbors a thick layer of organic haze. This unique feature has been the source of inspiration for many works regarding photochemistry and aerosol properties (Müller-Wodarg et al., 2014). The potential floatability of these aerosols, at the surface of Titan's seas, has been already discussed in an idealized, if not oversimplified, way (Cordier & Carrasco, 2019), and may have an enhanced wave damping effect, that could explain the radar and near-infrared, smooth aspect of these liquid bodies (Barnes et al., 2011; Cordier & Carrasco, 2019; Grima et al., 2017; Stephan et al., 2010; Wye et al., 2009; Zebker et al., 2014).

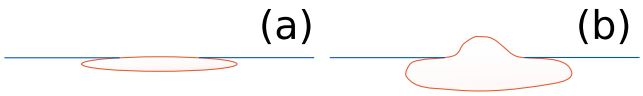

Figure 4. Panel (a) and (b): examples of solid particle shapes (in orange) that could float even with a very small contact angle.

Although the chemical composition of Titan's seas is only approximately known, reasonable estimates can be made, leading to a density around 500 kg m^{-3} and a surface tension of about ∼20 mN m^{-1} (Cordier et al., 2017). Laboratory determinations on Titan's aerosol analogs, called tholins (Sagan et al., 1992), lead to densities around ∼0.8 g cm^{-3} for high-pressure experiments (Hörst & Tolbert, 2013), and densities in the range 1.3–1.4 g cm^{-3} for low-pressure simulations (Brouet et al., 2016; Imanaka et al., 2012). However, for low-pressure measurements, densities can be found as small as 0.4 g cm^{-3} (Hörst & Tolbert, 2013), a value for which materials could simply float due to buoyancy forces. The wettability of aerosols remains essentially poorly constrained. Only a few derivations from measurements on laboratory analogs, are available. These determinations draw the picture of very wettable material with contact angle around $\theta_c = 5°$ (Rannou et al., 2019). A contact angle of strictly $\theta_c = 0°$ (Yu et al., 2020) is probably an idealization since it is not compatible with the conservation of mass principle. Titan's aerosols appear to be fractal aggregates of spherical monomers (Seignovert et al., 2017), for such a single sphere the use of Equation 2 leads to $R_{max} \sim 2 \times 10^{-4}$ m if we adopt a particle density of 10^3 kg m^{-3}, together with Titan's gravity $g_{Tit} = 1.352$ m s^{-2}. This estimate is well above the monomer radius estimations of ∼50 nm (Seignovert et al., 2017) enabling Titan's aerosol particles to float. We stress that these particles may have a variety of properties (chemical surface properties, size polydispersity, diversity of shapes, etc), leading to various floatabilities. In addition, when the contact angle is very small (e.g., a few degrees) a spherical particle would be almost fully immersed in the liquid, but according to Equation 3, only perturbations at frequencies above ∼500 MHz, which are unlikely, could destabilize the particle and make it sink. Then, the sea surface could be regarded as a "filter," trapping only a fraction of atmospheric sediments.

Finally, we recall that solid particles are not, by far, the only candidates for "floating microlayer builders" for Titan's seas. Molecules produced by chemical reactions in the Titan's atmosphere, like polyacetylenes (Chien, 1984; Elachi et al., 2005; Skotheim et al., 1998), are favored due to their low densities, while surfactant molecules like acrylonitrile (Stevenson et al., 2015) may also form thin monomolecular layers over the surface of the seas.

In the titanian case, other aspects have been also explored. For instance, the hypotheses of floating "pumices," made of very porous organic material to ensure buoyancy, has been proposed (Yu et al., 2024). Laboratory experiments have shown (Farnsworth et al., 2023) that non-coalescing liquid droplets may exist at the surface of methane-rich seas after hydrocarbon rainfalls. Interestingly, this phenomenon may appear to be independent of the liquid density. The floatation of ethane-rich drops is ensured in a wide range of sea bulk liquid compositions, while floating methane enriched droplets only exist in narrow ranges of composition and impact velocity.

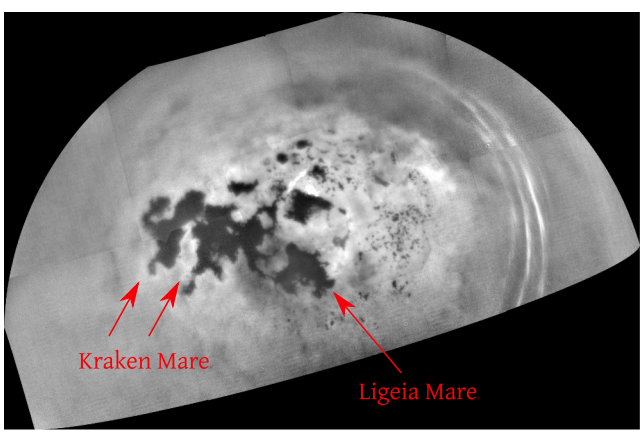

Figure 5. A mosaic of infrared images of Titan north polar regions taken by the Narrow Angle Camera of the ISS instrument aboard the Cassini spacecraft. The main hydrocarbon seas are clearly visible, their sizes are similar to those of the Great American lakes (Image Credit: NASA/JPL-Caltech/Space Science Institute).

2.2. The Case of Icy Moons Enceladus and Europa

While suspected since the early Eighties, when *Voyager* spacecrafts encountered Saturn's system, the existence of cryovolcanic activity on Enceladus has been revealed by *Cassini* spacecraft *Imaging Subsystem* (Porco et al., 2006). The plumes, material ejected from Enceladus' South Pole (see Figure 6), have been the subject of many works, and the analysis of their chemical composition showed a dominant role played by water vapor (Hansen et al., 2006, 2020); other simple molecules like CO_2, NH_3, H_2 and CH_4 contribute for less than ∼10% (Waite et al., 2009, 2017). Recently, the data acquired by the mass spectrometers onboard the *Cassini* spacecraft, lead to the detection of complex organic macromolecules, with masses above 200 atomic mass units (Postberg et al., 2018), like alkanes bearing more than 14 carbon atoms. These molecules have been found trapped in ice grains expelled by Enceladus' geysers. Whereas organic-free ice grains have a high salt concentration, those bearing organic material appear to be salt-poor grains. This latter type of grains does probably not reflect the composition of the Enceladus' salty ocean, in contrast with salt-rich grains generated by bursting of bubbles of volatile gas at water table. With molecular masses larger than 200 amu, organic compounds cannot leave the liquid phase or be embedded in the gas flux before condensating from the vapor. Alternatively,

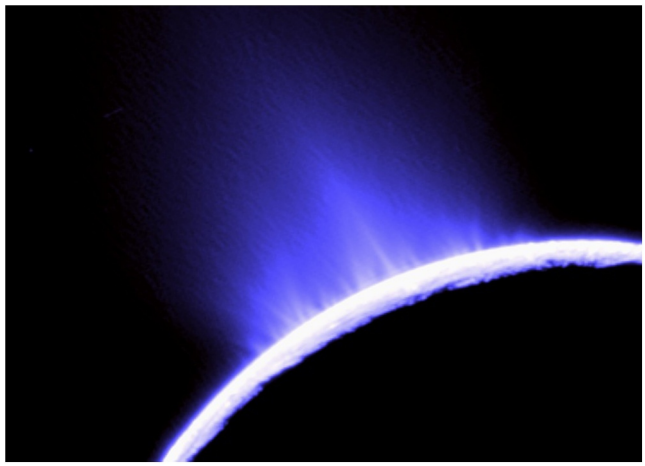

Figure 6. The plumes of ejected gases and icy dust from the south pole of the tiny moon Enceladus, whose diameter is approximately 500 km (Image Credit: Cassini Imaging Team/SSI/JPL/ESA/NASA).

if they would be dissolved in the water, we should have detected their presence in all grains. Hence, the proposed and most plausible scenario (Postberg et al., 2018) is the existence of a thin film or floating organic layer on top of the water table. Over the surface of the Earth's oceans, the formation of this kind of microlayer is a well known process with a dedicated literature (e.g., Gade et al., 2006).

The Enceladus subsurface water ocean is probably hidden below a ∼15 km thick icy shell (Schubert et al., 2007). At the interface between the liquid water and icy crust, the temperature should be around 273 K, with an hydrostatic pressure reaching 1.7 MPa. On its side, the gravity should not differ significantly from its surface value, that is, 0.11 m s^{-2}. Under these conditions the viscosity of liquid water remains around 1.6×10^{-3} Pa s (Pigott, 2011), because the influence of pressure appears negligible (Pigott, 2011). Similarly, the surface tension of water is expected to be close to the room conditions value, that is, 76 mN m^{-1} (Kalová & Mareš, 2018). On the Earth, there are countless examples of hydrophobic natural organic matter. For instance, in water treatment around 50% of organic compound present in raw water are hydrophobic (Kim & Yu, 2005). Due to darwinian selection processes, many biological surfaces are even superhydrophobic (X. J. Feng & Jiang, 2006).

Mechanisms at the origin of Enceladus organic compounds remain essentially unknown, but several hypotheses may be formulated. Carbonaceous chondrites are known to contain macromolecular organic compounds (Sephton, 2004; Sephton et al., 2003), materials which have been incorporated in the proto-Enceladus and altered afterward by hydrothermal processes. Organic compounds may also be generated through abiogenic processes, during fluid-rock interactions related to water circulation in Enceladus porous core (Choblet et al., 2017). Two main geochemical routes are mentioned in the literature: the serpentinization and the Fischer-Tropsch type synthesis (X. Wang et al., 2014). Both mechanisms may produce more or less complex hydrocarbons from a reservoir of CO and CO_2. Finally, the production of organic species by some sort of extraterrestrial form of life (Wagner et al., 2022) cannot be excluded.

Even if we are far to know the physical properties of Enceladus' organic material, some hints may be inferred from the properties of crude oils, that may be considered as relevant analogs.These substances are complex multicomponent mixtures containing a large quantity of hydrocarbons. Among hydrocarbons, the size of alkanes ranges roughly from C_5 to C_{40} (Chilingar et al., 2005), carbon chain lengths consistent with what we know about Enceladus. In general, raw petroleum is lighter than liquid water (e.g., Table 5.2 p. 94, Chilingar et al., 2005), only very heavy oils reach a density larger than 0.9, those above 1.0 exist but are rather rare (Zou, 2013). Concerning their wettability, hydrocarbons show generally a high hydrophobicity caused by the lack of polarity (Ström et al., 1987).

Taken globally, the mentioned arguments draw the surface of Enceladus ocean as a very favorable place for organic material floatability, even under the form of solid particles possibly denser than water. Quantitative estimations can be also made, for instance about the maximum radius of floating particles, by applying Equation 2. In a very unfavorable case, the density of the considered particle may be fixed to ∼1.2 times the value of the water density. The contact angle of paraffin (Ray & Bartell, 1953), namely ∼110°, offers a representative value for solid hydrocarbons, depending on surface state of the sample. Applying Equation 2, this angle leads to a maximum diameter of 12 cm. Therefore, we can conclude safely that any organic particle can float over the Enceladus water table surface, which appears as an ideal place for the formation of an organic floating film. This is a strong confirmation of the scenario proposed in the recent literature (Postberg et al., 2018), as an explanation for the presence of organics in a fraction of icy grains of South pole plumes.

Among galilean Jupiter's moons, Io is probably the only one without a subsurface water ocean (Greenberg, 2006). In the remaining three satellites, Europa has a particular place since its internal aqueous ocean (Vilella et al., 2020) is potentially connected to cryovolcanic activity (Roth et al., 2014; Sparks et al., 2017). In one decade, it will be explored by future space missions JUICE (Grasset et al., 2013) and Europa Clipper (Howell & Pappalardo, 2020), and possibly complemented by a Europa lander mission currently under study. According to thermal models, the temperature at the surface of Europa's ocean is close to 272 K and the pressure ranges from 10 to 50 MPa,

depending on the assumed icy crust thickness (Vilella et al., 2020). Compared to Enceladus, water viscosity and surface tension should remain roughly unchanged since the pressure is not enough enhanced to lead to significant changes. The major difference is the gravity that is around 1.3 m s^{-2}, that is, one order of magnitude larger than in the case of Enceladus. As a consequence, if some organic materials are also available at Europa water free surface; for a similar density and still according to Equation 2, floating particles should have a maximum size 3 times smaller than their Enceladean counterparts.

The list of solar system objects discussed above, potentially harboring a liquid phase, is obviously not exhaustive, since ocean worlds seem to exist in the outer solar system (Nimmo & Pappalardo, 2016). For instance, the Neptune's large satellite, Triton, has a surface where lava flows morphologic features have been identified (Croft et al., 1995), while geysers expelling nitrogen have also been observed (Soderblom et al., 1990). In this section, we have chosen to restrict our discussion to a few representative examples, supported by good observations and which could be explored in the near future.

3. Marine Capillary Waves

On a planetary science point of view, waves play an important role in ocean-atmosphere exchange of matter, heat, and momentum exchanges. Besides, they significantly contribute to costal erosion. Even though the question attracted the attention of scientists for centuries, the ocean waves generation remains a problem not fully understood in detail. This process is physically extremely complex: it involves an interface of two fluids of very different densities, the spatial scales vary from a few millimeters to kilometers, while time scales range from seconds to hours (Pizzo et al., 2021). This high variability is mainly due to the presence of turbulent flows in both fluids. Not surprisingly, the waves pull their energy from wind and the growth process follows 3 steps: (a) wind turbulence applies random stress variations on the surface, these pressure and tangential shear fluctuations give rise to wavelets, due to resonances in the wind-sea coupling (Miles, 1957; Phillips, 1957); (b) the wave amplitude is then reinforced by the air flow (Miles, 1957); (c) the waves start to interact among themselves, exciting longer wavelength modes (Komen et al., 1994). Recently, fully coupled direct numerical simulations were performed (J. Wu et al., 2022). Capillarity is prominent during the early stages of wave formation, and when some kind of water atomization appears (wave breaking, whitecap). The second aspect will be addressed in Section 4, since "*bubble bursting*" is recognized as a fundamental process for liquid water atomization. Here, we focus the discussion on the onset of wave generation, partially driven by capillarity. The natural angular frequency of the capillary wave on a free surface is given by (Lamb, 1993)

$$\omega_0^2 = \frac{\sigma k^3}{\rho_{\mathrm{liq}}} \tag{4}$$

where σ is the surface tension, k is the wave number of the capillary wave, and ρ_{liq} is the liquid density. It is difficult to go further without any of the properties of the wave "excitator," that is, the wind blowing over the sea surface. Nevertheless, Equation 4 draws clearly a difference between planetary bodies where the working liquid is methane and those harboring liquid water. The ratio $\sigma/\rho_{\mathrm{liq}}$ is found around 4×10^{-5} m^3 s^{-2} for liquid methane (relevant to Titan), for liquid water this value is about twice as large, that is, 7×10^{-5} m^3 s^{-2}. With these numbers we learn that, for a fixed wavelength, the wave growth should be facilitated by wind turbulences at different natural frequencies.

Due to the complexity of such air-liquid interactions, experimental approaches appear particularly relevant. Wind tunnel experiments, oriented to titanian and marsian planetary contexts were performed with the Mars Surface Wind Tunnel (Lorenz et al., 2005). These preliminary works suggested a strong dependence of capillary waves generation on atmospheric density, and waves on nonaqueous fluid surfaces looked more easily generated than on water. Another interesting discussion focussed on the Titan case, based on wind speed prediction provided by the TitanWRF Global Circulation Model and including the potential effects of viscosity and surface tension, was subsequently published (Lorenz et al., 2010). Unfortunately, the wind speeds computed over Titan polar regions, together with the properties of sea liquid are still too uncertain to yield definite conclusion. In the context of Cassini RADAR observations, a more sophisticated model of capillary-gravity waves on Titan's lakes has been proposed (Hayes et al., 2013), leading to prediction of waves detectability as a function of seasons. Unfortunately, these predictions were not corroborated by RADAR measurements.

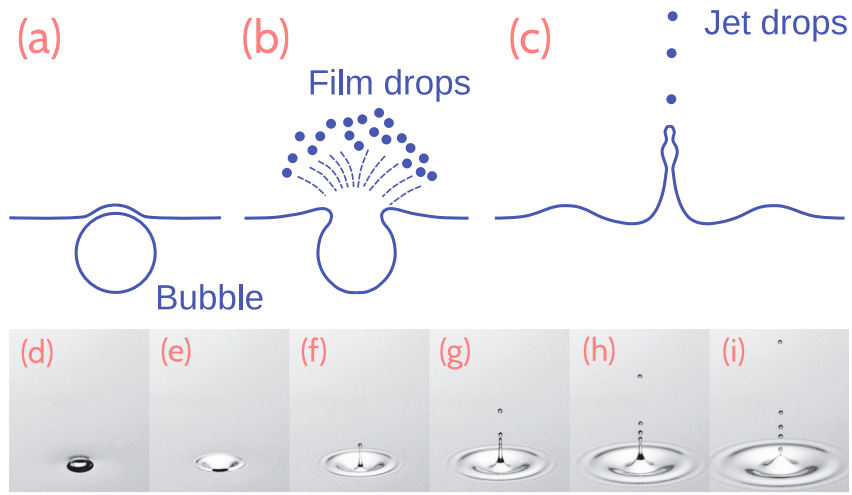

Figure 7. (a)–(c) Main steps of drops production during bubble bursting (inspired from Figure 3 in Resch et al. (1986)). (d)–(i) Time-sequence of a millimetric floating bubble bursting at the surface of pure water and propelling tiny jet drops above the surface (reprinted from Ghabache et al. (2014)).

For decades, researchers have been accumulating evidences or clues about the existence of very large areas of open water on the surface of Mars, during episodes of this planet geological history (Goudge et al., 2012, 2015). The case of wave formation at the surface of a Mars primordial ocean is even more puzzling since the properties of atmosphere in ancient geological times, particularly its density, are not well known. However, if Martian wave-cut shorelines could be confirmed, new constraints could be put on these properties (Adams, 2023; Banfield et al., 2015).

4. Bubble Bursting

Bubble bursting occurs in many natural and industrial processes, in physics, chemical and mechanical engineering, food science, geophysics, technology, medicine (Lohse, 2003) and oceanography, field which is the most relevant here. On the Earth, bubble bursting is recognized to have an essential role in sea-spray formation, which process is a major source of aerosols for the atmosphere at global scale and has a significant impact on the Earth's radiative balance and biogeochemical cycling (MacIntyre, 1972; X. Wang et al., 2017; Woodcock et al., 1953; J. Wu, 1981). Since the pioneering study of bursting bubbles conducted by Woodcock et al. almost 70 years ago (Woodcock et al., 1953), numerous experimental, numerical, and theoretical studies have been conducted with bubble bursting at a free surface. In brief, when a bubble reaches the free surface the residual liquid film on the top part (Figure 7a) breaks ejecting a myriad of tiny droplets, nicknamed "film drops" (Figure 7b), the cap collapse leading to the upward projection of the so-called Worthington jet, giving birth to larger "jet drops" (Figure 7c). As a result of the well-known Rayleigh-Plateau instability, the liquid jet breaks up into a few droplets called jet drops, as seen in the time-sequence displayed in Figures 7d–7i (Ghabache et al., 2014).

In recent decades, various scaling relations for the velocity, number and size of jet drops were reported in the literature. Nevertheless, it is only quite recently that much effort has been devoted to decipher minute details of the collapse of the immersed cavity leading to the production of jet drops during bubble bursting. Universal scaling laws relevant to the jet dynamics and drop size produced by bursting bubbles were thus recently proposed through combined experimental and numerical approaches (Berny et al., 2020; Deike et al., 2018; Ghabache & Séon, 2016; Ghabache et al., 2014; Séon & Liger-Belair, 2017). These universal scaling laws were retrieved by using dimensional arguments based on the three following dimensionless numbers: The Weber number $We = \rho V^2 R/\sigma$, which compares the effect of inertia and capillarity, the Bond number $Bo = \rho g R^2/\sigma$, which compares the effect of gravity and capillarity, and the Morton number $Mo = g\eta^4/\rho\sigma^3$, which only depends on the fluid properties. In the previous dimensionless numbers, V is either the jet velocity or the first jet drop velocity as it detaches from the tip of the jet, R is either the mother bubble radius or the resulting jet drop radius, g is the gravity acceleration, and μ, ρ and γ are respectively the liquid dynamic viscosity, density, and surface tension. By using dimensional arguments and a collection of dedicated experiments, the jet dynamics was described through

the following relationship, regime where the Morton number ranges over three decades ($10^{-11} \lesssim Mo \lesssim 10^{-8}$) (Ghabache et al., 2014; Séon & Liger-Belair, 2017):

$$We_d \simeq 3.9 \times 10^4 \times Mo^{2/7} \times Bo_b^{-1/2} \tag{5}$$

with the subscript b and d referring to the bubble and drop, respectively. The latter equation yields the following dependence of the jet tip (and first drop) velocity V_d with the mother bubble radius R_b and liquid parameters (expressed in SI units):

$$V_d \simeq 2 \times 10^2 \, \eta^{4/7} \, \sigma^{9/28} \, \rho^{-25/28} \, g^{-3/28} \, R_b^{-1} \tag{6}$$

In addition, in the same regime of Morton number, a scaling law was established between the Bond number of the first jet drop and a combination of both the Bond number of the bursting bubble and the Morton number as follows (Ghabache & Séon, 2016; Séon & Liger-Belair, 2017):

$$Bo_d \simeq 1.1 \times 10^{-5} \, Mo^{-1/3} \, Bo_b^{6/5} \tag{7}$$

Finally, the latter equation yields to the following dependence of the first jet drop size as a function of the initial bubble radius and liquid parameters (expressed in the SI units):

$$r_{\text{jet}} \simeq 3.3 \times 10^{-3} \, \eta^{-2/3} \, \sigma^{2/5} \, \rho^{4/15} \, g^{-1/15} \, R_b^{6/5} \tag{8}$$

The minimum size $r_{d,\min}$ of jet drops produced by bubble bursting may be roughly estimated (Brasz et al., 2018) by considering the Laplace number $La = \rho\sigma R_b/\eta^2$ which takes the particular value $La_{\min} \simeq 7 \times 10^3$ for the minimum ratio (Brasz et al., 2018),

$$\left(\frac{r_{\text{jet}}}{R_b}\right)_{\min} \simeq 4 \times 10^{-3} \tag{9}$$

allowing the derivation of $r_{jet,\min}$.

The production of film drops is a more complex mechanism not completely elucidated, even if fundamental works have been published on the topic (Bird et al., 2010). Laboratory and marine field studies have smaller diameters roughly ranging from 1 to 100 μm and above (Resch et al., 1986). While there are generally no more than ∼10 jet drops produced per bubble, the mean radius of film drops scales can be estimated using $\langle r \rangle_f \simeq R_b^{3/8} h_b^{5/8}/2$ and their number follows the law $N_f \simeq (R_b/l_c)^2 (R_b/h_b)^{7/8}$ with $h_b \simeq R_b^2/L$ where $L \simeq 20$ m on the Earth (Lhuissier & Villermaux, 2012). The term h_b represents the film thickness at the moment when the puncture occurs, the expression $h_b \simeq \mathcal{R}_b^2/L$ is explained by the convection within the film. Theoretical considerations lead to $L \simeq l_c/\epsilon^{1/2}$ where ϵ is the efficiency of film puncture by convective cell (empirically $\epsilon \simeq 1.8 \times 10^{-8}$ for tapwater in laboratory conditions). The minimum size of film drops can be evaluated using (Lhuissier & Villermaux, 2012)

$$r_{f,\min} \simeq \left(324 \, \frac{l_c}{L}\right)^{1/3} l_c \tag{10}$$

Another important aspect of bubble bursting is its ability to eject materials dissolved in the liquid or present at the surface under the form of a more or less thick films. This subject has been explored by many works focused on the terrestrial case since it has a great importance in marine aerosol formation. Depending on the exact nature of the organic material, particularly if it is soluble or not in the liquid, the organic material might be detected in all aerosol particles formed by bubble bursting or not. The behavior of soluble particles has been studied in many works in the context of the Earth (e.g., Bezdek & Carlucci, 1974; Chingin et al., 2018; Schmitt-Kopplin et al., 2012). Even if no general quantitative law has been found, it has appeared that marine spray formation tends to enrich, with respect to the bulk chemical composition, droplets in surface-active organic matter when water is the solvant.

The case of non-soluble compounds has been investigated in the context of oil spills (Ehrenhauser et al., 2014; Liyana-Arachchi et al., 2014), for which the ejection to the atmosphere of organic material has been also attributed to bubble bursting. However, the mechanism is slightly different because the alkanes are adsorbed at the liquid-air interface. Interestingly, the ejection of material trapped at this interface, via bubble bursting, seems to be independent of volatility and solubility of spill compounds.

4.1. The Case of Enceladus

As already recalled in Section 2.2, Cassini instruments detected the presence of water ice grains in Enceladus' South pole plumes. The total mass of grains has been determined to be ∼20% that of the water vapor (Dong et al., 2015). The sizes of these grains have been estimated with Cosmic Dust Analyzer aboard Cassini spacecraft which has a detection threshold around 0.2 μm (Postberg et al., 2011). With this instrument, a size distribution centered on a radius of ∼1 μm has been found (Postberg et al., 2018). Further investigations have been carried out with the Cassini Plasma Spectrometer (CAPS) and the Radio and Plasma Wave Spectrometer, the results have shown a grain size distribution peaked at ∼2 nm (Dong et al., 2015).

These icy grains have been divided into three categories (Postberg et al., 2009, 2011) according to their spectra: type I grains of almost pure water ice, type II grains containing a significant quantity of organic and/or siliceous material, and type III grains showing a very high salt concentration. Except for a portion of type I grains, which may be generated by homogeneous nucleation of icy crystals in the water vapor stream (Schmidt et al., 2008), the formation of other grains demands an atomization of the Enceladus watertable surface, and a freezing during their ascent in geyser cracks (Postberg et al., 2009). Such atomization may be obtained by two main processes: (a) a wave activity at the surface of liquid water, (b) bubble bursting of gases released by Enceladus core, or water vapor bubbles produced by surface boiling under low pressure.

On the Earth, ocean waves are a major source of water aerosolization (S. Liu et al., 2021). Such a wind-driven mechanism on Enceladus looks difficult to conceive. In contrast, processes based on bubble bursting appear much more plausible. In Enceladus plumes, the mixing ratio of water vapor ranges from 96% to 99% (Waite et al., 2017) and represents an evidence for an evaporation process at work. Other species have been also detected in Enceladus' geysers by the Ion Neutral Mass Spectrometer which was aboard Cassini, that is, CO_2, CH_4, NH_3, and H_2, likely released by hydrothermal activity in the satellite core. Thus, two categories of bubbles have to be distinguished: (a) bubbles containing the mentioned minor species originally formed in the core of Enceladus and traveling over tenth or hundredth of kilometers through the subsurface ocean, (b) the bubble of water vapor recognized to be generated within the few first tens of centimeters below the ocean surface by controlled boiling (Ingersoll & Nakajima, 2016). In the following, we discuss both cases, with a particular emphasis on subsequent sizes of droplets produced by bubble bursting.

4.1.1. Bursting of Bubbles Composed of Trace Gases

Coalescence, pressure drop, or diffusive feeding by dissolved gases may increase the size of bubbles up to their break-up radius R_{bk} (Cordier et al., 2017) during their ascent to the free surface. At Enceladus low gravity ($g_{Enc} = 0.113$ m s^{-2}), R_{bk} should be around 10 cm, one order of magnitude larger than the terrestrial value. The radius of subsequent jet drops produced by such big bubbles may be estimated using Equation 8, yielding $r_{jet,Enc} \sim 4$ cm. Even more striking is the corresponding minimum radius of jet drops given by Equation 9, around 0.2 mm. Finally, Equation 10 provides the minimum size of film droplets generated by Enceladus' mother-bubbles. The capillary length for Enceladus is around 2.5 cm, and if we assume that ϵ, the efficiency of film puncture by convective cell, has a universal value and that the bubble size is around 10 cm, the minimum film drop size should be around 8.8 mm. As a consequence, streams of bubbles, with sizes comparable to the break-up radius, produce liquid aerosols by bursting orders of magnitude too large to explain the observed sizes of Enceladus' geysers ice grains (∼1 μm). The bubbles initially formed in Enceladus' core, likely by heterogeneous nucleation, may have relatively small sizes, and their number per unit of volume of the subsurface ocean may be sufficiently low to impede significant coalescence, in such a way that bubbles reaching the free surface are tiny enough. However these circumstances remain very hypothetical, and do not impede other mentioned growth processes. Then, we have to review physical effects that could lead to small bubble bursting.

First, during their ascent to the free surface, bubbles undergoing a break-up event, produce an undetermined number of smaller bubbles. Several effects can potentially induce such break-up, for instance those driven by

hydrodynamics stresses or surface instabilities (Chu et al., 2019), but the corresponding size distribution cannot be evaluated. Second, bubble-bursting cascades may occur at sea surface. As show by laboratory experiments (Bird et al., 2010), following the rupture of the initial bubble, a ring of smaller bubbles can appear and the phenomenon may repeat, giving birth to a second generation of tiny bubbles. This two-step cascade seems to be able to reduce the diameter of bursting bubbles by two orders of magnitude (Bird et al., 2010), a diameter decrease which is not necessarily sufficient to get micro- or nano-metric ejected droplets.

Recently, a new mechanism based on the flapping shear instability has been proposed to explain the submicron drops in the context of the Earth oceans (Jiang et al., 2022). This mechanism seems to be efficient in producing film drops down to a few nanometers. Unfortunately, this process depends on the density ratio ρ_{air}/ρ_{liq} which has to be larger than $\sim 10^{-3}$. This condition is fulfilled in the terrestrial context with an air density around 1.2 kg m^{-3}, but on Enceladus, with a water vapor "atmosphere" it looks impossible. Right above the sea surface, the pressure can be at most equal to the water vapor pressure which is ~611 Pa at 0°C, corresponding to a density of 4.9×10^{-3} kg m^{-3}, well below the terrestrial air value. The required criterion is therefore not satisfied by around three orders of magnitude.

In sum, according to the general picture we have drawn about trace gas bubbles, we have to investigate other possibilities which could lead more confidently to the production of micrometric droplets.

4.1.2. Bursting of Water Vapor Bubbles

Concomitantly, the low pressure of the vapor phase right above the ocean causes the boiling of the very first layers of liquid, typical over a few tens of centimeters (Ingersoll & Nakajima, 2016). Unfortunately, we found very few references bringing information about the size distribution of these water vapor bubbles. In some laboratory works, related to nuclear power plant systems, the size of nucleating vapor bubbles seems to be around 0.5 mm (e.g., Kazuhiro et al., 2017) but the conditions are different compared to those of Enceladus ocean, particularly concerning the nature of nucleation sites. On Enceladus these sites should composed by water ice or organic material while in terrestrial experiments the solid substrates are made of steel or glass. This point is important since the size of bubbles leaving the nucleation substrate is related to the contact angle which depends on the chemical nature of the material (see for instance Giraud (2015)). It can be shown that, for a given horizontal solid surface, the detachment radius, that is, the value reached by the bubble when it leaves its substrate, is given by

$$R_{\text{detach}} \simeq \sqrt{\frac{3\sigma}{2\rho_{\text{liq}} g}} \sin\theta_c \tag{11}$$

with σ the surface tension and θ_c the contact angle. This equation is very similar to those proposed in the literature (Fritz, 1935; Giraud, 2015). The contact angle between water ice and liquid water appears to be very close to zero (Ketcham & Hobbs, 1969; Knight, 1971), leading to extremely small values for R_{detach}. If we assume, for instance, a contact angle of ~1°, Equation 11 leads to $R_{\text{detach}} \simeq 5.4 \times 10^{-4}$ m. The minimum size $r_{jet,min}$ of jet drops may be approached using Equation 9, this yields $r_{\text{jet, min}} \sim 2$ µm. Clearly, for a contact angle below 0.5°, jets generate submicron drops. The vertical velocity of such tiny bubble, in their ascent to the free surface, is very low and more than ~4 years can be required for a micrometer-sized bubble (Fifer et al., 2022) to cover a distance of ~71 cm (Ingersoll & Nakajima, 2016) through a quiet pool.

In fact, the first subsurface layers should be vigorously mixed by macroscopic convective eddies. We have identified several phenomena inducing mixing: The ascent of large bubbles coming from depths of Enceladus, which may drag the liquid and small water vapor bubbles, and the travel of centimetric methane bubbles through the last ~70 cm is around ~10 s. In addition, to maintain an evaporation flux, heat has to be transported from the ocean bulk to its surface. Otherwise, due to evaporative cooling, the surface freezes, stopping the geyser activity. Such a heat flux implies macroscopic convection. Finally, after evaporation, the remaining liquid water is cooler and more salty, therefore denser, and it should sink. Besides, during its journey to the surface, a tiny water vapor bubble should grow. The resulting size of water vapor bubbles bursting at the surface is the fruit of a competition between their growth and transport to the surface. Making an estimation of a relevant time scale is not easy. Nevertheless, the bubbles nucleating close enough to the surface will have a limited growth, and convection is characterized by eddies with non-uniform velocity distributions, letting the fastest eddies transport small bubbles with restricted growth. In conclusion, it is very plausible that bubbles of water vapor, small enough to produce

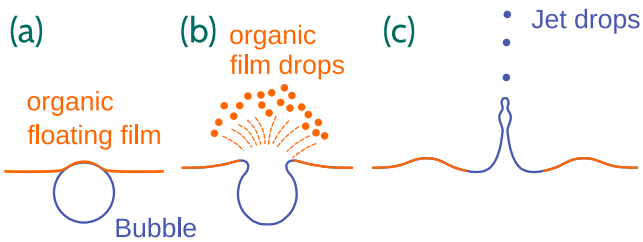

Figure 8. A conceptual illustration of bubble bursting in the presence of a surface floating film, this sketch follows essentially Figures 7a–7c. Cases (a) and (b) correspond to a situation where the thickness of the organic film is small compared to the bubble diameter, even if this film is not necessarily a monomolecular deposit. Here, only tiny film droplets of pure organic material are produced but, if the thickness of slick were larger than the bubble dimensions, jet drops would be also ejected.

micrometer-sized water droplets corresponding to film drop bursting, reach the water free surface within the Enceladus cracks, these liquid aerosols producing subsequently micrometer-sized icy grains.

Besides, organic materials may also be present at the surface of the Enceladus ocean, or in its immediate subsurface vicinity. Water vapor bubbles may also nucleate at these organic surfaces. In this case, the expected contact angle should be much larger than in the case of water ice, result which is particularly true when the organic matter is hydrophilic. For instance, with $\theta_c \sim 90°$, R_{detach} reaches 3 cm, corresponding to a minimum jet drops size above ~100 μm.

In closing, water vapor bubbling appears to be the most favorable process to produce water droplets small enough to account for the existence of micrometer-sized icy grains in the Enceladus geyser plumes, particularly in those containing salts.

4.1.3. Organic Matter Aerosolization

As already recalled in Section 2.2, organic materials probably colonize, at least partially, the water surface in Enceladus cracks. These organics could have been transported thanks to their own buoyancy, or drained from the moon deep interior by trace gases bubbles. The organic material could be molecules or small solid particles. In the first case, molecular surfactants can easily cover the surface of ascending bubbles; in the second case, a surface adsorption, driven by capillary forces as described in Sec. 2, can be invoked. As a consequence, organic deposits of various thickness could be built up at the water free surface, ranging from (a) organic layers thicker than bubble dimensions and (b) spills with a thickness large compared to molecular sizes but relatively small in comparison to the bubble diameters, to (c) molecular carpets. We can wonder how bubbles of water vapor, or containing trace gases, interact with these floating materials.

In the first case, depending on the physical state of the material (liquid or solid) and on the size of continuous pieces of matter, the interaction with bubbles will have a different character. The bubbles will not be able to go through a solid "organic pack," while their penetration in a floating organic liquid can be considered. The latter scenario is only valid for species still liquid at ~273 K, which should have a relatively small molecular weight. For instance, in the case of linear alkanes, the temperature of fusion (See the database https://webbook.nist.gov) remains below ~273 K for molecules with a chain shorter than C_{13} (tridecane). If the floating film has an horizontal extension much larger than the typical size of bubbles, then bubble-bursting may produce droplets of pure organic material (see Figure 8). In the situation hypothetized in Figure 8 sketch, laboratory experiments has brought to light the formation of a thin oily thread associated with jets during bursting in a system containing water covered by an oil film (Ji et al., 2021). This effect could generate small mesoscopic organic aerosols in the Enceladus context. In the case where the slick has a thickness larger than the typical size of bubbles, "pure" jet drops of organic may be produced. According to Equation 8, it is not obvious how the size of organic material jet drops could compare to their aqueous analogs since the organic liquid may be less viscous and less dense. However, the previous discussion about sizes of jet and film drops still applies to organic liquids, opening the possibility for the formation of small organic aerosols. If small enough, aerosol particles can be embedded in the vapor streams ascending along the cracks. During their journey, these drops can solidify and form small solid particles which could serve as water ice freezing nuclei. A similar reasoning may apply to floating solid phases: small enough solid particles may be embedded in geyser ascending streams, sticked to water droplets. We emphasized that mass spectra of organic materials have been found by Cassini instruments up to 1000–2000 u, and, due to the grain fragmentation in the instrument, the parent particles should have contained even many more larger particles (Postberg et al., 2018). This scenario is consistent with the existence of small solids.

A very interesting aspect has been revealed a decade ago by laboratory experiments: in the presence of surfactants in the water. An organic deposit at the liquid-air interface can lead to the production of nanoemulsions in the surface layers of the ocean (J. Feng et al., 2014). These nanoemulsions could take the form of submicrometer-sized organic droplets dispersed in the water, material that could be subsequently ejected into the air by bursting. The presence of the required surfactants has been suggested by plume measurements (Postberg et al., 2018).

Up to this point we did not consider the possible chemical fractionation between organic material at the surface of the ocean, and organic compounds aerosolized. We emphasized that this question is significantly different from that studied in recent investigations (Fifer et al., 2022), in which the relationship between plume composition and ocean composition is explored by ignoring bubble-bursting mechanisms. The possible chemical fractionation during bubble-bursting is still a matter of scientific debates. However some general trends may be drawn. For instance, concerning relatively thick slick, the fractionation should be a minor effect. This behavior is suggested by observations of oil spills on the Earth. In such event, bubbles are produced by breaking waves and it has been shown that the aerosolization of organic matter is practically independent of the vapor pressure and chain length of organic components (Ehrenhauser et al., 2014; Liyana-Arachchi et al., 2014). Excluding exceptional circumstances like oil spills, the biological activity enriches the sea surface layers with a plethora of organic species, and question of their transfer to aerosols has been largely studied, since this process has a major role in the physico-chemistry of the atmosphere, and influences the climate (e.g., Bezdek & Carlucci, 1974; Ganan-Calvo, 2022). It has been shown that surface active molecules tend to be overconcentrated in liquid aerosols compared to bulk water (Bezdek & Carlucci, 1974). This seems to be a general result. For instance it has also been found in studies dedicated to the effervescence of champagnes (Liger-Belair et al., 2009). In addition, a chemical fractionation appears to be at work (Chingin et al., 2018; Crocker et al., 2022; Schmitt-Kopplin et al., 2012). Such mechanisms could also be present on Enceladus, but it is difficult to disentangle what could be associated with mesoscopic or macroscopic, grain of organics, or with molecular floating films. Perhaps, far future space missions like *Exobiology Extant Life Surveyor* may bring clues on the topic. Nonetheless, bubble bursting is also a very plausible scenario for the existence of the Enceladus type II (organics rich) grains.

4.2. The Case of Titan

In the case of the Earth, the ocean surface agitation, through several atomization mechanisms, dominates the sea/atmosphere water exchange when the wind speed exceeds $\sim$15 m s^{-1} (Andreas et al., 1995). It is difficult to imagine such conditions over Titan's polar seas where marine surfaces are rather calm with an apparent absence of waves (Grima et al., 2017; Wye et al., 2009; Zebker et al., 2014). However, even if bubble bursting is not induced by breaking waves, streams of nitrogen rich bubbles may come into play (Cordier et al., 2017; Hofgartner et al., 2014, 2016). These bubbles could interact with postulated floating layers (Cordier & Carrasco, 2019), and propel material into the atmosphere. A similar process is at work on the Earth with marine biofilms which are sources of organic aerosols. Moreover, similarly to the Enceladus case, the relatively low gravity of Titan (1.352 m s^{-2}) should promote large bubbles, giving birth to large jet drops.

However, very noticeable differences between Titan and Enceladus or the Earth, are the nature of the liquid (liquid methane instead of water) and the density of the atmosphere in contact with the ocean. As already mentioned in Sec. 4.1.1, the flapping shear instability (Jiang et al., 2022), producing submicron film drops, in terrestrial environment, is expected to arise on Titan. Indeed, in this case $\rho_{air} \simeq 5$ kg m^{-3} and $\rho_{liq} \simeq 500$ kg m^{-3}, leading to the ratio $\rho_{air}/\rho_{liq} \simeq 10^{-2}$, one order of magnitude above the critical value of $\simeq 10^{-3}$ (see Figure 3A in Jiang et al. (2022)). This criterion has to be complemented by a second one: the radius of the mother bubble must be smaller than a fraction of the local capillary length ($\simeq$8 mm on Titan). In the case of Titan bubbles have to be subcentimetric, which is not a very restrictive condition. Indeed, the break-up diameter for bubble rising in Titan's seas is of the order of $\simeq$ 4.6 cm (Cordier et al., 2017), which has to be considered as a maximum value. Statistically it leaves space for populations of centimetric or subcentimetric bubbles. The theory of the "flapping shear instability" leads, for an initial gas bubble with a radius of 5 mm, to an average diameter of produced droplets around 30 μm. With a gravity and a liquid density lower than their terrestrial counterparts, the minimum vertical wind velocity to uplift a micrometric drop in the titanian atmosphere is around a few millimeters per second. This aspect opens the door to a potential redistribution of Titan's sea material at global scale extension. Any kind of sea molecule could be transported to any point of the titanian surface and be involved in microphysical processes of the atmosphere. Finally, this ocean-atmosphere interaction mechanism offers the possibility for global surface seeding by molecules generated/processed in the deep interior of Titan, and brought to its seas by geophysical phenomena like icy crust convection (Kalousova & Sotin, 2020). It can not be excluded that such molecules could be detected in regions explored by the *Dragonfly* mission.

5. Extraterrestrial Rain Droplets

The existence of an hydrological cycle has a huge impact on landscape morphology of planetary bodies. In the solar system only our planet, and one moon, Titan, are harboring such an active cycle at present. Besides, Mars exploration has revealed numerous evidences of a past hydrological activity. Indeed, ancient terrains of Mars preserve landscapes consistent with valley networks, lakes, alluvial fans, deltas (C. I. Fassett & Head, 2008; Howard et al., 2005; Hynek et al., 2010; Irwin et al., 2011) and possibly even oceans (Parker et al., 1993). These morphological features support the presence of liquid water flowing on the Martian surface during Late Noachian to Early Hesperian periods, ∼3.6 to 4 billion years ago. The widespread occurrence of clays is also a strong evidence for persistent water on ancient Mars (Bibring et al., 2006; Carter et al., 2015). A warmer and wetter climate than today, at least episodically, is required to explain these geologic evidences, with an active hydrological cycle. Nowadays, liquid water may exist in the depths of Mars (Lauro et al., 2021) or intermittently at its surface (Martín-Torres et al., 2015; Ojha et al., 2015). However, the current amounts involved are, by far, too small to sustain a hydrological cycle.

Generally speaking, and leaving aside the particular case of hail, rainfalls are the cycle phase during which water returns to the planetary surface. Due to the importance of weather predictions, the properties of rain droplets have caught the interest of scientists for a long time (Bentley, 1904; Loftus & Wordsworth, 2021; Marshall & Palmer, 1948). Since the interaction between raindrops and the soil depends on drop properties, we focus our attention on these properties.

5.1. Size Distribution of Rain Droplets

Probably the most salient and basic features of raindrops are their average size together with their size distribution. Early works focused on their experimental determinations (Laws & Parsons, 1943; Marshall & Palmer, 1948), lead to a number density of drops $n(d)$ (cm^{-4}), corresponding to sizes between d (counted as diameter) and $d + \mathrm{d}d$ per unit volume given by (Villermaux & Bossa, 2009)

$$n(d) = n_0 \exp(-d/\langle d \rangle) \tag{12}$$

with n_0 (cm^{-4}) a quantity reflecting the mean spatial density of drops, and $\langle d \rangle$ (cm) the average drop diameter. This distribution law compares nicely with empirical data for drop diameters $d \gtrsim 1$ mm. On the Earth, at ground level, the constant n_0 has a value around 0.08 cm^{-4} (Villermaux & Bossa, 2009), but it varies with temperature (Houze et al., 1979). The average diameter $\langle d \rangle$ is empirically related to the rainfall precipitation rate $\mathcal{R}$ ($\mathrm{mm\ h}^{-1}$) by

$$\langle d \rangle^{-1} = 41\, \mathcal{R}^{-0.21} \tag{13}$$

These laws have been confirmed by in situ measurements (Houze et al., 1979; Mason, 1971; Ulbrich, 1986) employing various methods, and is a broadly accepted result. The mean size of drops depends on the precipitation intensity: on average a heavy storm produces larger hydrometeors than a fine drizzle. Very interestingly, a quantitative explanation of prefactor and exponent values in Equation 13, based on first principles, is available in the literature (Villermaux & Bossa, 2009). Then, the developed formalism makes predictions possible for extraterrestrial contexts. In this frame, the precipitation rate $\mathcal{R}$ may be expressed as

$$\mathcal{R} = n_0 \frac{\pi}{6} \sqrt{\frac{\rho_{\mathrm{liq}}}{\rho_{\mathrm{air}}}} \sqrt{g}\, \langle d \rangle^{9/2} \int_0^{+\infty} x^{7/2} p(x)\, \mathrm{d}x \tag{14}$$

where the integral represents the shape of the drop size distribution and has an approximate value of 28.34 (Villermaux & Bossa, 2009). Other quantities are ρ_{liq} and ρ_{air}, respectively the liquid and the air densities ($\mathrm{kg\ m}^{-3}$), and g the gravity ($\mathrm{m\ s}^{-2}$). Parameters specific to the Earth yield to (Villermaux & Bossa, 2009)

$$\langle d \rangle^{-1} \simeq 48.5\, \mathcal{R}^{-2/9} \tag{15}$$

strikingly close to the empirical relation provided by Equation 13 ($2/9 \simeq 0.22$). If the fragmentation processes drive the size distribution of raindrop, the integral in Equation 14 with $x = d/\langle d \rangle$ and

$$p(x) = \frac{32}{3} x^{3/2} K_3(4\sqrt{x}) \tag{16}$$

should be universal and, consequently, it should not depend on the planetary context. Nevertheless, the pre-factor

$$f = \sqrt{\frac{\rho_{\text{liq}}}{\rho_{\text{air}}}} \sqrt{g} \tag{17}$$

depends on the planetary context. For our planet, we have the value $f_{\text{Earth}} \sim 90.4\ \text{m}^{1/2}\ \text{s}^{-1}$, while for Titan $f_{\text{Titan}} \simeq 10.8\ \text{m}^{1/2}\ \text{s}^{-1}$ (for numerical inputs, see Cordier et al. (2017)). Thus, for a fixed precipitation rate $\mathcal{R}$, the value of f factor suggests mean raindrop diameter $\langle d \rangle \simeq 1.6$ times larger in Titan's rainfalls. Another quantity, relevant for raindrops features, is the maximal size d_{max} of a stable drop given by (Villermaux & Bossa, 2009)

$$d_{\text{max}} = \sqrt{\frac{6\sigma}{\rho_{\text{liq}} g}} \tag{18}$$

yielding a diameter of 6 mm in the terrestrial case, while for Titan we get $d_{\text{max}} \simeq 1.3$ cm. This evaluation, not dependent on the precipitation rate, reinforces the picture of larger raindrops on Titan. This result is consistent with early estimations (Lorenz, 1993) based on similar principles.

The case of early Mars is more tricky since the thermodynamic conditions (pressure and temperature in its atmosphere of CO_2-H_2O), that prevailed in this epoch are not well established (Ramirez et al., 2014). Nitrogen and argon isotope compositions, measured in the Martian meteorite Allan Hills 84001, provide a lower limit of 0.5 bar for the atmospheric ground pressure 4 billion years ago on Mars (Kurokawa et al., 2018). Of course, the existence of liquid water requires a temperature around 273 K. The value of the ground pressure is more uncertain, but a range between 0.5 and 4 bar appears to reasonably bracket the real values (Craddock & Lorenz, 2017; Ramirez et al., 2014). Relevant numerical values yield a ratio $f_{\text{Mars}}/f_{\text{Earth}}$ in between 0.3 and 0.7. As a consequence, for an equivalent precipitation rate $\mathcal{R}$, the average droplet diameter should be only ~20% larger in the early Mars context than on our nowadays planet. Concerning the raindrop maximal size, we found for Mars $d_{\text{max}} \simeq 1$ cm, roughly twice as large as the diameter of terrestrial drops. This estimation is consistent with previous determinations (Craddock & Lorenz, 2017), particularly if we take into account the statistical significance of such an assessment.

Here, both estimations, for Titan and Mars, have been made assuming a similar parameter n_0. The parameter n_0 and precipitation rate $\mathcal{R}$ depend on the details of precipitation microphysics, and more generally on the global behavior of the atmosphere. In the following, we examine several possible geophysical consequences of large raindrops.

5.2. Raindrop-Induced Erosion

With tectonic activity and volcanism, erosion is one of the major geophysical processes that shape a planetary landscape. Erosion cannot be reduced to a single phenomenon, it can be governed by chemical dissolution or induced by mechanical effects (Lorenz & Lunine, 1996). On the Earth, erosion is caused by many phenomena combining the effects of winds, precipitation or runoff of liquid water, and the effects of water ice during freezing or melting. Raindrop splash can be seen as the first step in erosion of soil by rainfalls. Unfortunately, even the erosion provoked only by rainfalls depends on endless parameters: soil erodibility, slope steepness, rainfall rate, etc (Caracciolo et al., 2012; Gholizadeh et al., 2018; Y. Wang et al., 2020). All these parameters, empirically determined in the terrestrial case, are absolutely unknown, even when they could be relevant, in extraterrestrial environments. The only aspect we can discuss here is the raindrop kinetic energy which is a parameter involved in raindrop-induced erosion, since it characterizes the strength of the impacts, and the ability of a droplet to detach particles from soil. For ease of comparison, we have adopted d_{max} (see Equation 18) as the size of a droplet and the velocity of falling is provided by the terminal velocity (Lorenz, 1993)

Figure 9. An example of fossil raindrop imprints on the top of a wave-rippled sandstone from the Horton Bluff Formation (Mississippian). This sample is on display at the Blue Beach Fossil Museum (Hantsport, Nova Scotia). Picture taken by Michael Rygel, publicly shared under Creative Commons Attribution-Share Alike 3.0 Unported license.

$$U = \sqrt{\frac{2m_{\text{drop}}g}{\rho_{air}SC_d}} \tag{19}$$

with the mass of the raindrop $m_{\text{drop}} = \pi\rho_{\text{liq}}d^3/6$, the drag reference area S and the drag coefficient C_d (Clift et al., 1978). The deformation due to aerodynamic forces has been taken into account for the estimations of both S and C_d (Lorenz, 1993). A slightly different drag parametrization may be found in more recent works (Loftus & Wordsworth, 2021).

In the case of the Earth, we found $U_{\text{Earth}} \simeq 9$ m s^{-1}, and a terminal kinetic energy $K_{\text{Earth}} \simeq 4.5$ mJ. For Titan, the relevant numerical inputs lead to $U_{\text{Titan}} \simeq 1.5$ m s^{-1} and $K_{\text{Titan}} \simeq 0.65$ mJ. Finally, in the Marsian context we have considered two values of pressure (i.e., 0.5 and 4 bar, see Section 5.1) yielding respectively $U_{\text{Mars}} \simeq 7.8$–$2.6$ m s^{-1} and $K_{\text{Mars}} \simeq 10^{-2}$–$1.1$ mJ. All other parameters remaining equal, the maximum kinetic energy for raindrops seems to be significantly lower in the context of Titan than in that of Mars or the Earth. However, it remains much larger than the erosivity threshold, that is, the minimum kinetic energy (around a few μJ) required to initiate soil particle detachment as experimentally determined for fine sand and silt loam (Salles et al., 2000). These estimations suggest possible weaker raindrop-induced erosion on Titan, compared to the Earth or Mars, but it is impossible to be more conclusive in the present state of our knowledge. Titanian erosivity thresholds for relevant organic analogs should be measured in laboratory; but, river bed networks observed on Titan indicate that significant erosion by runoff has been at work in the past.

We emphasize that the kinetic energy mentioned here is a drop individual quantity and does not include, the precipitation rate as it was done in other estimations (Whitford & Duval, 2020).

5.3. Raindrop Imprints

A disdrometer is an instrument able to determine raindrop sizes and velocity distributions. In the absence of such a device on a planetary probe, one has to search for rainfall artifacts. On the Earth, fresh raindrop imprints in dusty or sandy terrains may be routinely observed. Fossil records have also been reported and used to constrain the air density existing billion years ago (Som et al., 2012), or to provide a way of retrodeforming plant or animal fossils (Fichman, 2013). An example of terrestrial fossil raindrop impressions is displayed in Figure 9. Extraterrestrial surfaces may also preserve more or less ancient traces of rainfalls.

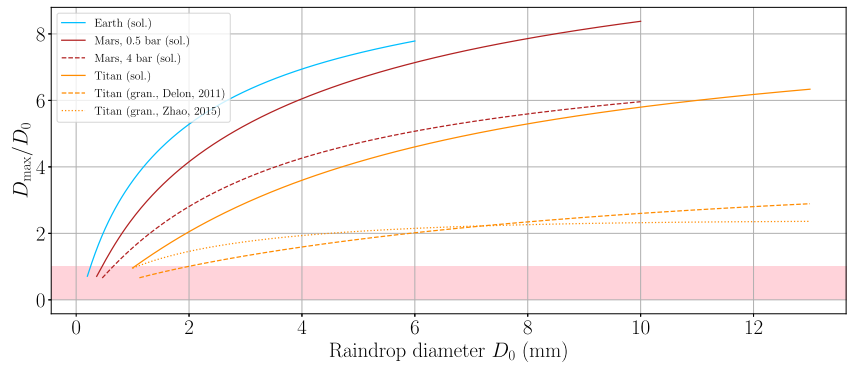

Figure 10. The ratio D_{max}/D_0, with D_{max} the maximum diameter of a raindrop of initial diameter D_0, spreading when impacting a solid surface ("sol." label). Two atmospheric pressures have been considered in the case of Mars. We have also plotted curves showing the variations of D_{max}/D_0 when a raindrop impacts a granular medium ("gran." label), the corresponding prescriptions have been found in Delon et al. (2011) and Zhao et al. (2015). For the latter a "packing fraction" of 0.58 has been hypothesized for the sand. Both laws are variations of the type $D_{max}/D_0 \propto We^{1/4}$. The pinkish shade emphasizes the area where the raindrop deforms itself but not frankly "splashes" since $D_{max}/D_0 \lesssim 1$.

As a first approach, we restrict our discussion to an idealized scenario where a droplet hits a smooth and flat horizontal surface. Immediately after the impact, under the effect of inertia the liquid spreads circularly, this spreading is countered by the capillary and viscous forces (Roisman et al., 2002). We let D_{max} be the maximum diameter of the spreading, and D_0 the diameter of the droplet in flight. A universal scaling law, that is, applicable to all regimes (capillary and viscous), may be found by introducing the impact parameter $P = We\mathrm{Re}^{-2/5}$, where $We = \rho_{liq} D_0 U^2/\sigma$ is the Weber number which compares inertial and capillary forces. The quantity $\mathrm{Re} = \rho_{liq} D_0 U/\eta$ represents the well known Reynolds number, accounting for the ratio between inertial and viscous forces. This law, allowing an excellent fit to empirical data, may be written as (Laan et al., 2014)

$$\frac{D_{max}}{D_0} = \mathrm{Re}^{1/5} \frac{P^{1/2}}{A + P^{1/2}} \tag{20}$$

with A a "universal" dimensionless constant, empirically determined: $A = 1.240 \pm 0.001$. Equation 20 connects the size distributions of raindrops and impacts on a solid surface. In Figure 10 we have gathered results relevant for Titan, the Earth and Mars. The raindrop minimum diameter $D_{0,\,min}$, considered in this figure, is determined by the condition $We \gtrsim 1$. Indeed, for $We < 1$ the raindrops are not really "splashing," but are rather gently deposited since the capillary forces dominate inertial ones, the deformation remains mild. The maximum diameters of in-flight raindrops $D_{0,\,max}$, have been fixed in accordance with Equation 18. All raindrop terminal velocities, required in Re and We evaluations, have been evaluated following the procedure described in Section 5.2. The D_{max}/D_0 appears to be an increasing function of D_0 (see Figure 10), reflecting the growing dominant effect of inertia during impact, compared to the effect of surface tension. In the vicinity of $D_{max}/D_0 = 1$ the fate of a landing raindrop is probably governed by capillary interaction with the soil and/or by evaporation (see Sec. 6). In this region the droplets deviate from the strict application of Equation 20. Moreover, for a fixed raindrop diameter the deformation during the impact is smaller on Mars (at least in the low pressure atmosphere) and Titan compared to what happens on the Earth. This is mainly caused by lower terminal velocities in the marsian and titanian cases.

Up to this point, the rain-vector has been assumed to be perpendicular to the impacted surface, hypothesized horizontal. The literature provides procedures to take into account inclined targeted surfaces (Laan et al., 2014).

More importantly, planetary surfaces are often covered by granular media: sand, regolith, sedimented aerosols, etc. These materials are known to exhibit behavior that cannot be approximated by a continuous solid. Then, the crater resulting from a raindrop impact on such granular medium should be different from what we get on a solid surface, at least in terms of spatial extension. The physics of the impact of a liquid droplet on a granular structure, is still the subject of active researches. Such a system is rather complex since it intricates the properties of the liquid and those of its targeted material; nonetheless a general behavior can be drawn. Assuming a full transfer of the drop-granular impact energy to the drop surface, leads to $D_{max}/D_0 \propto We^{1/2}$ (Zhao et al., 2015). However,

recent works agree with a law of the type $D_{max}/D_0 \propto We^{1/4}$ (Delon et al., 2011; Katsuragi, 2010; Zhao et al., 2015). This power law is explained qualitatively by energy dissipation in internal degrees of freedom of the drop, and by the energy required for sand excavation. The effect of granular medium properties, such as the ratio of granular medium/water densities (Katsuragi, 2010) or the packing fraction of the powder (Zhao et al., 2015) might be discussed but these details would not change drastically the overall conclusion. In Figure 10, we have plotted examples of $D_{max}/D_0 \propto We^{1/4}$ laws (see the two lower curves) only in the case of Titan for clarity. As expected, raindrop spreading during impact on a sandy terrain is significantly smaller than in the case of a solid surface. Interestingly, the plotted laws converge to relatively mild deformation with a maximum around $D_{max}/D_0 \simeq 3$. The average slopes of these curves are also smaller than those obtained for solid surface impacts, letting the raindrop size distribution less altered. This aspect is rather favorable to the use of sediment raindrop imprints, as a constraint on atmosphere microphysics.

5.3.1. Application to Titan

The *Cassini* spacecraft has revealed many evidences for the existence of a hydrological cycle based on liquid methane on Titan. For instance, a lot of images of fluvial patterns have been acquired (Langhans et al., 2012; Le Gall et al., 2010), suggesting the occurrence of rainfall events in the past. Cloud activity has been clearly brought to light (Turtle et al., 2018), but the observations of rainfalls have been scarce. Although such observations are more likely to be done in polar regions which appear to be the wettest, their in situ exploration belongs to the far future even if several mission concepts have been already proposed (e.g., Rodriguez et al. (2022)). Such observations are not excluded during the timespan of the *Dragonfly* mission, which is dedicated to equatorial regions, namely relatively dry regions according to GCM models (Lora et al., 2019). Two episodes of rain showers have been identified during the *Cassini* era: one in South polar regions (Turtle et al., 2009) and another in the equatorial zone (Turtle et al., 2011). In any case, the search for fossil raindrop imprints is perfectly relevant for *Dragonfly* which plans to investigate soils in environments rich in sediments (Lorenz et al., 2021). The impact of raindrops could happen on a flat solid surface in the natural surroundings of the probe, or even on its own hull; alternatively droplets may fall, or may have fallen, on a granular soil leaving more or less persistent traces. At the time of writing these words, we do not know if a flat and horizontal part of the *Dragonfly* fuselage will be accessible to camera fields of view. Beside clues concerning the raindrop size distribution based on D_{max}/D_0 measurements, the observation of liquid drops deposited on a human made surface could bring information about the properties of the liquid, particularly via the contact angle determination. We emphasize that pre-flight empirical studies of probe surface wettability, by liquid methane (and other relevant mixtures), could be very useful to in situ observations since low velocity droplet deposition and final state on the surface, depend on the surface wettability. As shown in Figure 10, liquid methane raindrop imprints in Titan sediments, recently formed or fossilized, may constitute interesting pieces of information on Titan processes which produce liquidometeors. The situation is all the more favorable as the drop sizes should be relatively little altered according to estimations reported in Figure 10. Flat geological surfaces, possibly covered by a thin layer of organic dust, could be the perfect target for the mentioned investigations. The existence of such targets is plausible in interdune regions which are planned to be explored by *Dragonfly* (Lorenz et al., 2021). Such structures could be imaged by instruments belonging to the *Dragonfly Camera Suite* (*DragonCam* for short, Lorenz et al. (2018)) that includes a microscopic imager able to characterize surface objects down to sand-grain scale. Finally, we underline that hail may also reach the surface of Titan (Graves et al., 2008), but observational evidences of such event are still not available. More generally, other erosion processes are at work on Titan's surface, like eolian and chemical processes. Discussions may be found in the literature (Lorenz & Lunine, 1996).

5.3.2. Application to Mars

In contrast to Titan, today Mars climate is particularly dry, leaving no hope for rainfall observations. However, the Marsian weather may have undergone rainy episodes ~3.6 to 4 billion years ago, and sedimentary deposits may have recorded artifacts of these events.

Orbital detection of clay stratigraphies on early Martian terrains is best explained if Mars experienced a period between the mid-Noachian (>3.85 Gy) and the end of the Noachian (~3.7 Gy) during which climatic conditions allowed persistent liquid water on its surface (Carter et al., 2015). Rainfall may have occurred during this time period due to the resulting hydrological cycle of evaporation-precipitation, which is correctly modeled by the

most recent 3D global climate simulations (Turbet & Forget, 2021). Therefore, the mudstone sediments formed on early Mars could have recorded raindrop imprints.

The Mars Science Laboratory Curiosity rover landed in Gale crater on 6 August 2012. Gale crater formed near the time of the Noachian to Hesperian transition, ∼3.61 Gy ago (Le Deit et al., 2013). In situ observations indicate deposits attributed to a stream and a delta, marking the boundary of an ancient lake (Grotzinger et al., 2014). Infilling began shortly after the crater formed and ended in the early Hesperian, likely ∼3.3 to 3.2 Gy (Grant et al., 2014). The older outcrop explored by Curiosity rover, namely Sheepbed mudstones, is interpreted as formed by settling of primary grains in a lake (Grotzinger et al., 2014). It could have recorded raindrop imprints at a time when it was exposed to the atmosphere, as a coastal environment for instance, and to rainfall. However, the climatic conditions during the lake formation are important, as a too cold climate would result in snowfall instead of rainfall. Although morphological features indicate possible periglacial processes with a permafrost environment after the first hundred thousand years following the crater formation (Le Deit et al., 2013), there is no evidence for a cold climate environment when the lake was present (Grotzinger et al., 2014). The Curiosity rover is equipped with a set of 17 scientific and engineering cameras which can provide complementary information on photographed raindrop imprints. The two Navigation Cameras (Navcam) acquire panoramas of the surroundings of the rover after each drive. They can resolve features of about 9 mm in size at 2 m. The front and rear Hazard Avoidance Cameras (Hazcam) take pictures on a daily basis and can resolve features down to ∼7 mm in size. The Mast Camera (Mastcam) instrument is capable of resolving features of ∼2 mm at a distance of 2 m with its 34 mm focal length lens, and ∼0.8 mm at 2 m with a lens of 100 mm focal length (Bell et al., 2017; Malin et al., 2017). However, the field of view covered by the mosaics taken by these cameras is rarely as large as for the Navcam mosaics, except for the 360° Mastcam mosaics. The Remote Micro-Imager is part of the ChemCam instrument aboard Curiosity rover. It can resolve features down to ∼200 μm in size (Le Mouélic et al., 2015) and is mainly used to document the geological context of the Laser-Induced Breakdown Spectrometer measurements. Finally, the Mars Hand Lens Imager (MAHLI) is a contact instrument mounted on the turret at the end of Curiosity's 2 m-long robotic arm (Edgett et al., 2012, 2015). MAHLI can resolve objects 45 − 60 μm in size. The Curiosity rover has imaged hollow nodules on Sheepbed mudstone (Grotzinger et al., 2014). These are mm-scale circular rims with hollow centers. They have mean diameters of 1.2 mm, and minimum/maximum diameters of 0.6/5.6 mm. So far, the interpretation of these hollow nodules involves either the dissolution of the inner material, creating the void space, or gas bubbles formed during or soon after deposition of mudstone (Grotzinger et al., 2014).

The Mars 2020 Perseverance rover landed in Jezero crater on 18 February 2021. Jezero crater formed during mid-Noachian, with an age greater than 3.82 Gy (Sun & Stack, 2020). Jezero crater has been interpreted as a paleolake (C. Fassett & Head, 2005) containing a prominent fan-shaped body of sedimentary rocks deposited on its western margin (Schon et al., 2012). On the basis of images taken by the Perseverance rover, the sedimentary deposits of this Gilbert-type delta indicate a transition from sustained hydrological activity in a persistent lake environment to highly energetic short-duration fluvial flows (Mangold et al., 2021). The fluvio-lacustrine deposits, containing clay minerals (Horgan et al., 2020), could have recorded raindrop imprints in the past. Among the instruments available on Perseverance rover, the two Navcam cameras are well suited for raindrop imprints photography since they acquire panoramas of the surroundings of the rover after each drive and can resolve features ∼3.3 mm at a distance of 2 m. The Mastcam-Z, consisting in two identical cameras mounted on the Perseverance remote sensing mast, is capable of resolving features down to ∼0.7 mm in size in the near field at the 110 mm focal length setting.

As part of China's first Mars exploration mission "Tianwen-1," the Zhurong rover touched down on the surface of southern Utopia Planitia on 15 May 2021. The Zhurong rover is equipped with a multispectral camera (MSCam) which is probably the most capable instrument for our purpose since it can resolve features ∼1.5 mm in size. However, the region explored by the Zhurong rover has an age of ∼3.45 Gy (Late Hesperian) (X. Wu et al., 2021), when the Martian climate was very likely too cold for rainfalls. Furthermore, the landing area was resurfaced around the Middle Amazonian and the materials on the current terrain could be as young as ∼700 My (J. Liu et al., 2022) with no possible observations of raindrop impressions.

6. Raindrop Absorption by a Porous Soil

On the Earth, the soil physics is an important topics (Lal & Shukla, 2004) since properties of soils have significant consequences on the water cycle. In extraterrestrial contexts, Titan is the only body where one could observe

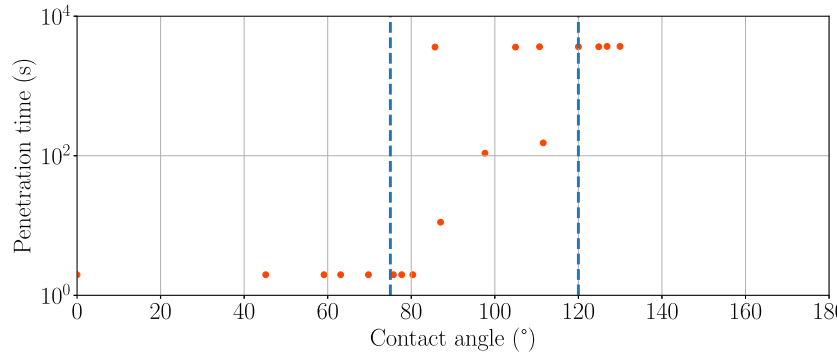

Figure 11. Penetration time of water in a soil as a function of the contact angle, data read in Figure 6 of Bachmann et al. (2003).

rainfall events in the next decades; thus we will restrict our discussion to this moon. The *Dragonfly* quadcopter is planned to explore a region over which large quantities of organic materials have sedimented. The presence of porous terrains is therefore likely and precipitations of liquid methane (see Section 5.3.1) may be absorbed by the soil.

As a first approach, a porous medium may be idealized as a large number of vertical parallel cylinders randomly distributed (Hilpert & Ben-David, 2009). Right after its deposition on such a medium, a droplet of liquid starts to flow downward, filling up the "tubes." The temporal evolution of the length $h(t)$ of the liquid slug in "tubes" may be approached by the implicit non-linear equation (Hilpert & Ben-David, 2009; Washburn, 1921)

$$\frac{h}{h_0} - \frac{t}{t_0} = \ln\left(1 + \frac{h}{h_0}\right) \tag{21}$$

with the length scale $h_0 = 2\sigma \cos\theta_c/\rho g R_p$ and the time scale $t_0 = 16\sigma\eta \cos\theta_c/\rho^2 g^2 R_p^3$ where η, σ, ρ, g and R_p are respectively the dynamic viscosity (Pa s), the surface tension (N m^{-1}), the density (kg m^{-3}), the gravity (m s^{-2}) and the radius (m) of the "pores" of the substrate. The numerical resolution of Equation 21 gives results qualitatively comparable with t_{abs} (Hapgood et al., 2002)

$$t_{\text{abs}} = 1.35 \frac{\eta V_d^{2/3}}{\sigma \epsilon^2 R_p \cos(\theta_c)} \tag{22}$$

where ϵ is the porosity of the granular medium and V_d the initial volume of a drop deposited on the considered medium. In Equation 22, large porosity and pore radius favor short absorption times, while we have the opposite behavior by increasing the liquid viscosity and the drop volume. Obviously, an equation like (22) is valid only for liquidophilic substrates, and this absorption time gets longer for the most liquiphobic material since $t_{\text{abs}} \propto 1/\cos(\theta_c)$. This tendency is confirmed by measurements acquired on the Earth soils (see Figure 11) where the absorption time is very long for liquidophobic materials.

On Titan, if the deposition of raindrops on a porous soil occurs in the zone explored by *Dragonfly*, the observations could enable us to distinguish between liquidophilic and liquidophobic materials. The disappearance of raindrops should be ruled by droplet penetration in liquidophilic soils and droplet evaporation in liquidophobic soils. The time scale of methane absorption due to the soil liquidophily, as derived from Equation 21, is a fraction of second for a 2 cm methane raindrop, whereas the evaporation should take ~10 hr according to empirical evaporation rates (Luspay-Kuti et al., 2015). The type of observations suggested here should be feasible with *Dragonfly* which is equipped with cameras and sensors measuring the air pressure, temperature, wind speed and "humidity" (methane abundances) available in the *Dragonfly Geophysics and Meteorology Package* (DraGMet) (Lorenz et al., 2018). The detection of "methanophobic" material sedimented at the surface of Titan is important due to its potential role in marine floating formation over polar seas (Cordier & Carrasco, 2019).

The investigations could be even pushed forwards if the soil porosity or the pore dimension are assessed by *Dragonfly* electromagnetic or optical measurements, since the numerical resolution of Equation 21 could lead to an estimation of the contact angle θ_c.

7. Conclusion

Given the incredible ubiquity of capillary processes at play in terrestrial environments, we have reviewed and discussed some of them with possible importance in planetary contexts of our solar system. Having this common theme as a guideline, we have paid special attention to effects which could be directly or indirectly observed during near future space missions, or are of particular conceptual relevance. Of course we made choices and this work is not exhaustive, some other aspects could have been discussed, for instance the acoustic expression of bubble population in extraterrestrial waterfalls (Leighton & White, 2004), bubble formation due to heat leak or cavitation around a boat or a submarine (Cordier, 2016; Hartwig et al., 2016), or soil adhesion due to organic mud, in which capillarity induced the formation of liquid bridges between solid particles (Lorenz, 2022).

We have confirmed that the surface of Enceladus ocean is likely to be the most favorable place of our planetary system for organic matter flotation. As it is the case in numberless terrestrial situations, the "bubble bursting" is probably at the origin of the extraction, and concentration, of this material in tiny water droplets embedded in the flux of vapors ascending into geysers conduits. Concerning this "bursting," two distinct populations of bubbles can emerge at the interface between the liquid ocean and the vapor flux: (a) bubbles containing minors species (CO_2, CH_4, …) coming from the deep interior, (b) bubbles of water vapor, formed at shallow depth with a size almost arbitrarily small when released from their nucleation site. Since the very low gravity of Enceladus promotes large bubbles, and subsequently centimetric jet drops, the observed icy grains are likely to have been produced either by particular phenomena as cascade bursting of large bubbles (of CH_4, CO_2, …), or by bursting of tiny water vapor bubbles. The involved chemo-physical mechanisms have to be clarified; this is the reason why laboratory experiments of liquid water, close to 273 K, boiling under low pressure are highly desirable. Such investigations would be of particular interest in the perspective of *Europa Clipper* mission that could confirm the existence of geysers on Europa. This relevance is even reinforced in the case of the future in situ exploration of Enceladus.

The Titan's low gravity, combined with the nature of the working liquid, that is, mainly liquid methane, favor bubbles and drops of sizes much larger than in the terrestrial context. The determination of size distributions would provide valuable information about the microphysics of the titanian low altitude atmospheric layers. Even if the areas which will be visited by *Dragonfly* are recognized to be rather dry, the observation of "fossil raindrop imprints" is technically possible with *Dragonfly* instruments. Similar observations would be feasible on Mars, nonetheless they remain unlikely in view of the configuration of current Martian missions. The detection of raindrops, or dewdrops, on titanian ground would offer the opportunity to characterize soils (e.g., the liquidophily of organic material sedimenting from the atmosphere).

As hypothesized in previous works, the hydrocarbon seas of Titan are prone to be covered, at least partially, by layers of organic materials sedimenting from the atmosphere. The nature of these layers may range from monomolecular to much thicker deposits. About organic grains, their size is a key parameter to assess their propensity to float. Liquidophilic material could lead to floating matter provided that the particle size is small enough. Although preliminary laboratory works have already been conducted, more in depth investigations are required since this scientific question may have potential important consequences for Titan at global scale. Indeed, we have demonstrated (see Section 4.2) that even in the absence of "breaking waves" at the surface of Titan's maria, the production of micronic aerosols may be driven by an aspect of bubble bursting called "flapping shear instability" which is likely to occur in the Titan's context.

This bubble bursting specific mechanism is conceptually important since it makes possible the injection into the atmosphere of material previously processed in the interior of Titan. While cryovolcanism activity (Lopes et al., 2013) and cratering (Neish & Lorenz, 2012) could represent rare or very rare events, bubble bursting offers an alternate route to convey a broad variety of chemicals from the interior of Titan to its atmosphere. The well identified maria and lacus are not the only sites where bursting could occur. The transient presence of liquid hydrocarbons flushing the ground (MacKenzie et al., 2019; Malaska et al., 2022) may be imagined in other regions, due to precipitations or dynamics of the local "alkanofer" (Cordier et al., 2021). Fluxes of gases may, in such a situation, induce bubble-bursting, at the origin of the production of aerosols.

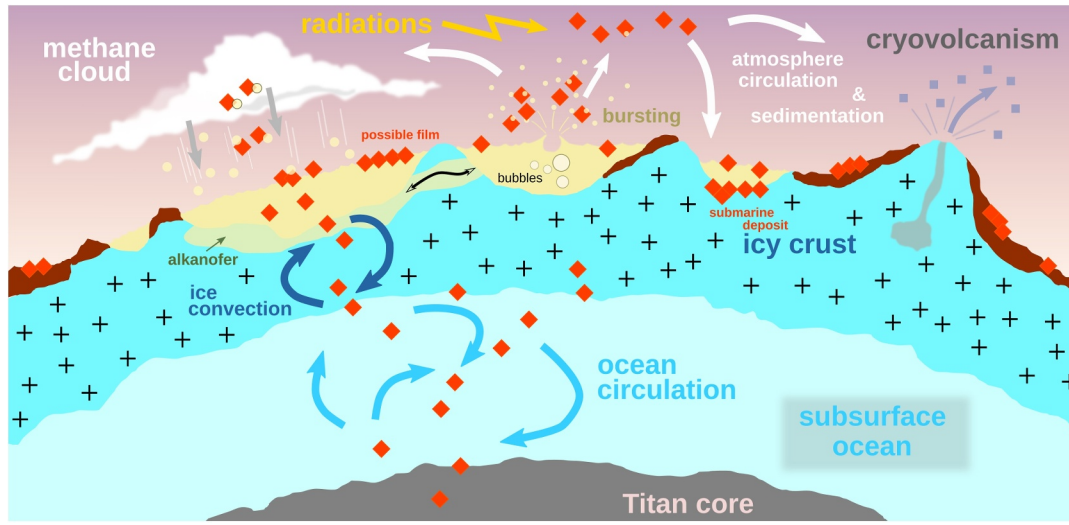

Figure 12. A schematic view of a "meta-cycle" showing organic material traveling between the deepest regions of Titan's interior, to the high altitude atmosphere, before going back to the moon core. The external part of nowadays Titan core is probably made of high pressure water ice (Sotin et al., 2021). For the sake of simplicity, the particles of organic material are represented by a unique type of orange diamond, but their nature can evolve during the course of their "meta-cycle." In each compartment organic matter is transported by the circulation of fluids, or semi-fluids in the case of icy crust. In a few environments, the material can be transformed, for instance by radiations in the atmosphere or by hydrolysis in the subsurface water ocean. In the atmosphere, organic particles can play the role of nucleation seeds for the formation of crystals or liquid droplets. The organic compounds can form floating films at the surface of lakes/seas, or sink to the bed, from which they could be lifted off by marine circulation or bubbles streams. The bubble bursting may inject tiny droplets and organics in the air. The presence of alkanofers could ensure a form of communication between lakes. Finally, we have also represented massive organic layers at the surface (in brown), and the possible cryovolcanism that could also provide the atmosphere with subsurface materials. The bubbling activity processes may have played a role in the emergence of molecular superstructures like azotosomes, one first step toward exobiological activity.

Below the surface, a succession of transport phenomena could take turns with each other: the subsurface aqueous ocean ensures the interaction with Titan core and the external icy crust (Sotin et al., 2021), this ocean being surely well mixed by the convection. The deep core is probably a region rich in organic compounds, surrounded by a convecting high pressure ice shell. The convection in the icy crust could transport material from the ocean free surface up to a few kilometers above it (Kalousova & Sotin, 2020). Finally, the liquid circulation in an "alkanofer" (Cordier et al., 2021; Faulk et al., 2020; Horvath et al., 2016) could release compounds directly to the surface or in a sea acting as an intermediate between the "alkanofer" and the atmosphere. Of course, matter transportation in the opposite direction, that is, from the atmosphere to the inner regions of Titan's interior, is easily conceivable. Once put together, all these elements draw a global picture of a large "meta-cycle" made of a few "environmental niches" in interaction. Such a "meta-cycle" has already been advocated by Lerman with his theory of the "Bubble-Aerosol-Droplet Cycle," nicknamed "bubblesol cycle" in the context of the terrestrial emergence of life (Lerman, 1986; Lerman & Teng, 2005). We propose an adaptation of this "meta-cycle" to Titan as sketched in Figure 12. This meta-cycle is an entanglement of several sub-cycles harbored in the atmosphere, the seas, the alkanofers, the crust and the water global ocean. In all these compartments, the transported material can be subject to chemo-physical changes. For instance, the organic substances, originally produced in the atmosphere, or coming from the deep core of Titan, could be altered during their journey in the interior, undergoing hydrolysis in the aqueous ocean (Neish et al., 2009, 2010). Re-injected in the atmosphere by bubble-bursting and atomized in micronic particles, they can be transported downwind or higher in the atmosphere, and deposited in areas like those visited by *Dragonfly*.

Up to this point, we have emphasized the role of bubble-bursting as a mechanism of aerosols production, seeding the whole surface of Titan with material coming from the interior. However, bubble bursting has also two other effects that could be of paramount importance: (a) it can selectively desolvate organic compounds with mole fraction as low as 10^{-9}; for instance, the concentration of materials dissolved in water was found to be increased by a factor of 10^4 after desolvation (Lerman & Teng, 2005); (b) in presence of surface active molecules, the production of tiny droplets promotes the formation of bilayer vesicles which are prerequisites for the emergence of life similar to the terrestrial ones (Chang, 1993; Schulze-Makuch & Irwin, 2018).

The effect of selectivity and concentration of compounds in droplets produced by bursting is well known when the solvent is water, and similar effect can be expected with a cryogenic solvent mainly based on methane. Once in the air, each micronic droplet can behave like a micro-reactor in which chemical reactions are favored. Energy deposition on the droplet may even accelerate processes.

All forms of life we know on the Earth are compartmentalized: multicellular organisms are, by definition, composed of several entities bounded by a membrane, bacteria are structured by a molecular wall (the cytoplasmic membrane) while equivalently viruses have their capsids. The self-emergence of these "molecular walls" may have been favored, or catalyzed, by the presence of bubbles in the primordial seas. These ideas have already been discussed decades ago (Chang, 1993) in works according to which bubble formation, and bursting at the surface, may be seen as a plausible mechanism for closing vesicles. The production of synthetic liposomes, based on bubbling, has also been proposed by the pharmaceutical industry (Talsma et al., 1994). The appearance of membrane promoted by bubbles may be advocated in both Titan- and Enceladus-like environments.

The "meta-cycle," proposed for Titan, can be also envisaged for Enceladus where a part of the material blowed off by geysers is deposited over Enceladean surfaces (Robidel et al., 2020). The considered layer may be subsequently transported back to the ocean with the help of the icy crust convection. More localized sub-cycles may be devised. Inside cracks, right above the water surface, bursting could favor the formation of vesicles and higher concentrations, which will finally go back to the ocean surface.

In this work, we have focused our discussion on solar system objects whose liquid phases will be available to observation and exploration in upcoming decades. During the beginning of its operations, the JWST has already shown the possible existence of water on the exoplanet WASP-96 b, while the hunting for exomoons is at its premises (Kipping et al., 2022). The detection of stable liquid phases on these classes of objects is a promising field (Maltagliati, 2019; Trees & Stam, 2019). However, detailed studies of capillarity effects in such objects will remain a distant dream for a long time yet.

Appendix A: Conditions for Floatability by Capillarity

In this frame, let us define a spherical solid particles; of radius R and density ρ_{sol}. This object is assumed to be deposited at the surface of a liquid characterized by a density ρ_{liq} and a surface tension σ (see Figure A1). According to the literature (Lee, 2018), this particle undergoes three forces. The most obvious of them, is the weight

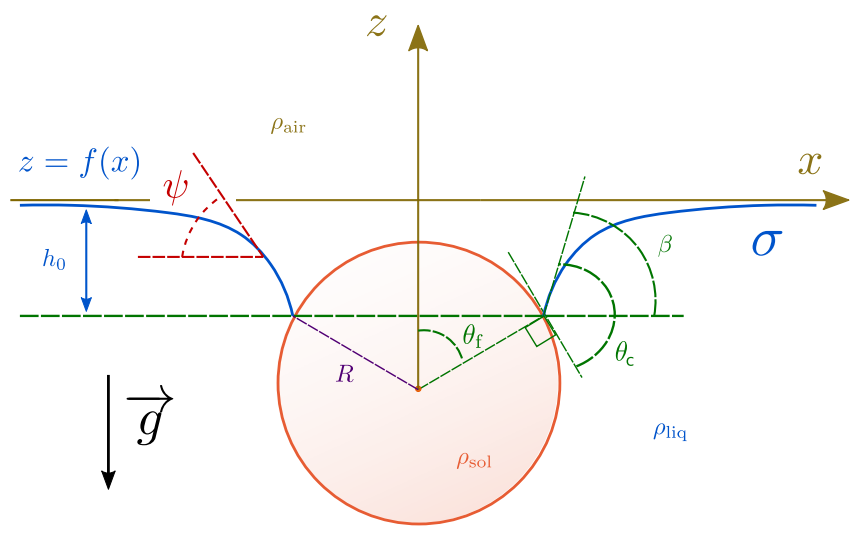

Figure A1. Sketch of a spherical solid particle, of radius R and density ρ_{sol}, floating at the surface of a liquid with density ρ_{liq}. The meniscus (blue line) is represented by the equation $z = f(x)$, the surface tension of the interface is σ, while the contact angle between the solid and the liquid is denoted θ_c; θ_f is the filling angle. The difference of height between the plane of flotation and the surface of the unperturbed liquid is h_0. The local tangent to the meniscus has the angle ψ with the horizontal direction. The gravity is represented by $\vec{g}$. This figure is our reconstruction of Figure 1 published by Lee (2018), it is also very similar to Figure 2 in Scheludko et al. (1976).

$$F_M = \frac{4\pi}{3}\rho_{\text{sol}} R^3 g \tag{A1}$$

The second one is the capillary force, whose vertical component F_C has the expression

$$F_C = 2\pi R \sin\theta_f \,(\sigma \sin\beta) \tag{A2}$$

where θ_f is the filling angle and β includes both the contact angle θ_c and θ_f (see Figure A1: $\beta = \theta_c - \theta_f$). Taking into account forces caused by air and liquid, coming from the classical Archimede's principle, and also generated by liquid above the line of flotation (i.e., corresponding to the "layer" of thickness h_0 in Figure A1), the resulting buoyancy force is

$$\begin{aligned} F_B = \frac{4\pi}{3} R^3 \rho_{\text{air}} g + \frac{\pi}{3} R^3 \left(2 + 3\cos\theta_f - \cos^3\theta_f\right) \times \\ \left(\rho_{\text{liq}} - \rho_{\text{air}}\right) g - \pi R^2 \sin^2\theta_f \, h_0 \left(\rho_{\text{liq}} - \rho_{\text{air}}\right) g \end{aligned} \tag{A3}$$

The flotation of the particle is reached at equilibrium when we have the force balance

$$F_M = F_C + F_B \tag{A4}$$

Unfortunately, this equation cannot be solved alone since it contains two unknowns: the filling angle θ_f and h_0; other parameters, particularly the contact angle θ_c, specify the nature of the system, and are assumed to be given. As a requirement, we have to include the Young-Laplace equation

$$\kappa_m = \frac{\rho_{\text{liq}} - \rho_{\text{air}}}{2\sigma} g z \tag{A5}$$

which governs the profile of the meniscus (blue line in Figure A1). In this equation, κ_m is the local mean curvature given by the non-linear differential equation

$$\kappa_m = -\frac{1}{2}\left(\frac{f''}{(1+f'^2)^{3/2}} + \frac{f'}{x(1+f'^2)^{1/2}}\right) \tag{A6}$$

where $z = f(x)$ is the equation of the meniscus profile. According to the dedicated literature (Lee, 2018), the system of Equations A4–A6 can be reformulated under the form of a pair of differential equations, solved numerically using a shooting method (Lee, 2018). In Figure 3a we show an example of computed menisci profiles, illustrating the influence of the density ratio $D = (\rho_{\text{sol}} - \rho_{\text{air}})/(\rho_{\text{liq}} - \rho_{\text{air}})$. By expanding and reformulating Equation A4, we can write

$$\frac{g}{6\sigma}\left(\rho_{\text{liq}} - \rho_{\text{air}}\right) R^2 = \frac{\sin\theta_f \sin\left(\theta_c - \theta_f\right)}{4D - \left(2 + 3\cos\theta_f - \cos^3\theta_f\right) + 3\frac{h_0}{R}\sin^2\theta_f} \tag{A7}$$

Since, in the present context, the density of the solid is larger than the liquid one, the ratio D remains larger than 1 (a typical value is around ~2); in addition, we have $-2 \le 3\cos\theta_f - \cos^3\theta_f \le +2$ for all the permitted θ_f values, which are in the range $0° - 180°$. As a consequence, the denominator of the right-hand side of Equation A7 is positive. Then, the liquid being denser than the air, $\sin(\theta_c - \theta_f)$ has to be positive and, importantly, the filling angle θ_f has to remain smaller than the contact angle θ_c.

For $\theta_f \lesssim 45°$, the term $3\cos\theta_f - \cos^3\theta_f$ remains reasonably close to 2, and $3h_0/R \sin^2\theta_f$ is negligible, in such a case

$$\frac{g}{6\sigma}\left(\rho_{\text{liq}} - \rho_{\text{air}}\right) R^2 \simeq \frac{\sin\theta_f \sin\left(\theta_c - \theta_f\right)}{4D - 4} \tag{A8}$$

It can be easily shown (Crawford & Ralston, 1988; Scheludko et al., 1976) that the radius has a maximum value $R_{\max}$ for $\theta_f = \theta_c/2$ and

$$R_{\max} \simeq \sqrt{\frac{3\sigma}{2(\rho_{\text{sol}} - \rho_{\text{liq}})\, g}} \sin\frac{\theta_c}{2} \tag{A9}$$

Data Availability Statement

The computer software developed for this work is publicly available in the Zenodo archive (Cordier, 2023).

Acknowledgments
We gratefully acknowledge the Reviewers Dr. Ralph Lorenz and Pr. Jason Barnes for their very constructive suggestions that improved significantly our manuscript. We thank Gabriel Tobie and Benjamin Charnay for scientific discussion, and Michael Rygel for sharing his fossil raindrop imprint picture. The present research was supported by the Programme National de Planétologie (PNP) of CNRS-INSU co-funded by CNES, and also partially supported by the HPC center of Champagne-Ardenne (ROMEO). This work has been done mainly using open-source softwares like `Python`, `gfortran`, `kate`, `Jupyter Notebook`, LATEX under `GNU/Debian Linux` operating system. The authors warmly acknowledge the whole Free Software community.

References

Adams, K. D. (2023). Wind, waves, sediment transport, and potential for shoreline development on Earth and on Mars. *Icarus*, *405*, 115695. https://doi.org/10.1016/j.icarus.2023.115695

Andreas, E. L., Edson, J. B., Monahan, E.-C., Rouault, M. P., & Smith, S. D. (1995). The spray contribution to net evaporation from the sea: A review of recent progress. *Boundary-Layer Meteorology*, *72*(1–2), 3–52. https://doi.org/10.1007/bf00712389

Bachmann, J., Woche, S. K., Goebel, M.-O., Kirkham, M. B., & Horton, R. (2003). Extended methodology for determining wetting properties of porous media. *Water Resources Research*, *39*(12), 1353. https://doi.org/10.1029/2003WR002143

Banfield, D., Donelan, M., & Cavaleri, L. (2015). Winds, waves and shorelines from ancient martian seas. *Icarus*, *250*, 368–383. https://doi.org/10.1016/j.icarus.2014.12.001

Barnes, J. W., Soderblom, J. M., Brown, R. H., Soderblom, L. A., Stephan, K., Jaumann, R., et al. (2011). Wave constraints for Titan's Jingpo Lacus and Kraken Mare from VIMS specular reflection lightcurves. *Icarus*, *211*(1), 722–731. https://doi.org/10.1016/j.icarus.2010.09.022

Bell, J. F., Godber, A., McNair, S., Caplinger, M. A., Maki, J. N., Lemmon, M. T., et al. (2017). The Mars Science Laboratory Curiosity rover Mastcam instruments: Preflight and in-flight calibration, validation, and data archiving. *Earth and Space Science*, *4*(7), 396–452. https://doi.org/10.1002/2016EA000219

Bentley, W. (1904). Studies of raindrops and raindrop phenomena. *Monthly Weather Review*, *10*, 450–456.

Berny, A., Deike, L., Séon, T., & Popinet, S. (2020). Role of all jet drops in mass transfer from bursting bubbles. *Physical Review Fluids*, *5*(3), 033605. https://doi.org/10.1103/physrevfluids.5.033605

Bezdek, H. F., & Carlucci, A. F. (1974). Concentration and removal of liquid microlayers from a seawater surface by bursting bubbles1. *Limnology and Oceanography*, *19*(1), 126–132. https://doi.org/10.4319/lo.1974.19.1.0126

Bibring, J.-P., Langevin, Y., Mustard, J. F., Poulet, F., Arvidson, R., Gendrin, A., et al. (2006). Global mineralogical and aqueous Mars history derived from OMEGA/Mars Express data. *Science*, *312*(5772), 400–404. https://doi.org/10.1126/science.1122659

Bird, J. C., de Ruiter, R., Courbin, L., & Stone, H. A. (2010). Daughter bubble cascades produced by folding of ruptured thin films. *Nature*, *465*(12), 759–762. https://doi.org/10.1038/nature09069

Brasz, C. F., Bartlett, C. T., Walls, P. L. L., Flynn, E. G., Yu, Y. E., & Bird, J. C. (2018). Minimum size for the top jet drop from a bursting bubble. *Physical Review Fluids*, *3*(7), 074001. https://doi.org/10.1103/PhysRevFluids.3.074001

Brouet, Y., Levasseur-Regourd, A. C., Sabouroux, P., Neves, L., Encrenaz, P., Poch, O., et al. (2016). A porosity gradient in 67P/C-G nucleus suggested from CONSERT and SESAME-PP results: An interpretation based on new laboratory permittivity measurements of porous icy analogues. *Monthly Notices of the Royal Astronomical Society*, *462*(Suppl 1), S89–S98. https://doi.org/10.1093/mnras/stw2151

Caracciolo, C., Napoli, M., Porcù, F., Prodi, F., Dietrich, S., Zanchi, C., & Orlandini, S. (2012). Raindrop size distribution and soil erosion. *Journal of Irrigation and Drainage Engineering*, *138*(5), 461–469. https://doi.org/10.1061/(asce)ir.1943-4774.0000412

Carter, J., Loizeau, D., Mangold, N., Poulet, F., & Bibring, J.-P. (2015). Widespread surface weathering on early Mars: A case for a warmer and wetter climate. *Icarus*, *248*, 373–382. https://doi.org/10.1016/j.icarus.2014.11.011

Chang, S. (1993). Prebiotic synthesis in planetary environments. In J. Greenberg, C. Mendoza-Gómez, & V. Pirronello (Eds.), *The chemistry of Life's origins* (pp. 259–300). Springer.

Chien, J. C. W. (1984). *Polyacetylene: Chemistry, physics, and material science*. Academic Press.

Chilingar, A., Buryakovsky, L. A., Eremenko, N. A., & Gorfunkel, M. V. (2005). *Geology and geochemistry of oil and gas* (1st ed.). Elsevier.

Chingin, K., Yan, R., Zhong, D., & Chen, H. (2018). Enrichment of surface-active compounds in bursting bubble aerosols. *ACS Omega*, *3*(8), 8709–8717. https://doi.org/10.1021/acsomega.8b01157

Chipfunhu, D., Massimiliano, Z., & Grano, S. (2011). The dependency of the critical contact angle for flotation on particle size – Modelling the limits of fine particle flotation. *Minerals Engineering*, *24*(1), 50–57. https://doi.org/10.1016/j.mineng.2010.09.020

Choblet, G., Tobie, G., Sotin, C., Běhounková, M., Čadek, O., Postberg, F., & Souček, O. (2017). Powering prolonged hydrothermal activity inside Enceladus. *Nature Astronomy*, *1*(12), 841–847. https://doi.org/10.1038/s41550-017-0289-8

Chu, P., Finch, J., Bournival, G. S. A., Hamlett, C., & Pugh, R. J. (2019). A review of bubble break-up. *Advances in Colloid and Interface Science*, *270*, 108–122. https://doi.org/10.1016/j.cis.2019.05.010

Clift, R., Grace, J. R., & Weber, M. E. (1978). *Bubbles, drops and particles*. Academic Press.

Cordier, D. (2016). How speed-of-sound measurements could bring constraints on the composition of Titan's seas. *Monthly Notices of the Royal Astronomical Society*, *459*(2), 2008–2013. https://doi.org/10.1093/mnras/stw732

Cordier, D. (2023). Terminal velocity and splashing of extraterrestrial raindrops [Software]. *Zenodo*. https://doi.org/10.5281/zenodo.10391618

Cordier, D., Bonhommeau, D. A., Vu, T. H., Choukroun, M., & García-Sánchez, F. (2021). Vertical compositional variations of liquid hydrocarbons in Titan's alkanofers. *Astronomy & Astrophysics*, *653*(A80), A80. https://doi.org/10.1051/0004-6361/202140789

Cordier, D., & Carrasco, N. (2019). The floatability of aerosols and wave damping on Titan's seas. *Nature Geoscience*, *12*(5), 315–320. https://doi.org/10.1038/s41561-019-0344-4

Cordier, D., García-Sánchez, F., Justo-García, D. N., & Liger-Belair, G. (2017). Bubble streams in Titan's seas as a product of liquid N_2 + CH_4 + C_2H_6 cryogenic mixture. *Nature Astronomy*, *1*(5), 0102. https://doi.org/10.1038/s41550-017-0102

Craddock, R. A., & Lorenz, R. D. (2017). The changing nature of rainfall during the early history of Mars. *Icarus*, *293*, 172–179. https://doi.org/10.1016/j.icarus.2017.04.013

Crawford, R., & Ralston, J. (1988). The influence of particle size and contact angle in mineral flotation. *International Journal of Mineral Processing*, *23*(1–2), 1–24. https://doi.org/10.1016/0301-7516(88)90002-6

Crocker, D. R., Kaluarachchi, C. P., Cao, R., Dinasquet, J., Franklin, E. B., Morris, C. K., et al. (2022). Isotopic insights into organic composition differences between supermicron and submicron sea spray aerosol. *Environmental Science & Technology*, *56*(14), 9947–9958. https://doi.org/10.1021/acs.est.2c02154

Croft, S. K., Kargel, J. S., Kirk, R. L., Moore, J. M., Schenk, P. M., & Strom, R. G. (1995). The geology of Triton. In *Neptune and triton* (pp. 879–947).

de Gennes, P.-G., Brochard-Wyart, F., & Quéré, D. (2004). *Capillarity and wetting phenomena: Drops, bubbles, pearls, waves*. Springer. https://doi.org/10.1007/978-0-387-21656-0

Deike, L., Ghabache, E., Liger-Belair, G., Das, A. K., Zaleski, S., Popinet, S., & Séon, T. (2018). Dynamics of jets produced by bursting bubbles. *Physical Review Fluids*, *3*(1), 013603. https://doi.org/10.1103/PhysRevFluids.3.013603

Delon, G., Terwagne, D., Dorbolo, S., Vandewalle, N., & Caps, H. (2011). Impact of liquid droplets on granular media. *Physical Review E*, *84*(4), 046320. https://doi.org/10.1103/PhysRevE.84.046320

Dong, Y., Hill, T. W., & Ye, S. Y. (2015). Characteristics of ice grains in the Enceladus plume from Cassini observations. *Journal of Geophysical Research: Space Physics*, *120*(2), 915–937. https://doi.org/10.1002/2014JA020288

Drelich, J. W., Boinovich, L., Chibowski, E., Della Volpe, C., Hołysz, L., Marmur, A., & Siboni, S. (2020). Contact angles: History of over 200 years of open questions. *Surface Innovations*, *8*(1–2), 3–27. https://doi.org/10.1680/jsuin.19.00007

Edgett, K. S., Caplinger, M. A., Maki, J. N., Ravine, M. A., Ghaemi, F. T., McNair, S., et al. (2015). Curiosity's robotic arm-mounted Mars Hand Lens Imager (MAHLI): Characterization and calibration status (Technical Report). *MSL MAHLI Technical Report*.

Edgett, K. S., Yingst, R. A., Ravine, M. A., Caplinger, M. A., Maki, J. N., Ghaemi, F. T., et al. (2012). Curiosity's Mars Hand Lens Imager (MAHLI) Investigation. *Space Science Reviews*, *170*(1–4), 259–317. https://doi.org/10.1007/s11214-012-9910-4

Ehrenhauser, F. S., Avij, P., Shu, X., Dugas, V., Woodson, I., Liyana-Arachchi, T., et al. (2014). Bubble bursting as an aerosol generation mechanism during an oil spill in the deep-sea environment: Laboratory experimental demonstration of the transport pathway. *Environmental Sciences: Processes & Impacts*, *16*(1), 65–73. https://doi.org/10.1039/C3EM00390F

Elachi, C., Wall, S., Allison, M., Anderson, Y., Boehmer, R., Callahan, P., et al. (2005). Cassini radar views the surface of Titan. *Science*, *308*(5724), 970–974. https://doi.org/10.1126/science.1109919

Farnsworth, K. K., Soto, A., Chevrier, V. F., Steckloff, J. K., & Soderblom, J. M. (2023). Floating liquid droplets on the surface of cryogenic liquids: Implications for Titan rain. *ACS Earth and Space Chemistry*, *7*(2), 439–448. https://doi.org/10.1021/acsearthspacechem.2c00311

Fassett, C., & Head, J. W. (2005). Fluvial sedimentary deposits on Mars: Ancient deltas in a crater lake in the Nili Fossae region. *Geophysical Research Letters*, *32*(14), L14201. https://doi.org/10.1029/2005gl023456

Fassett, C. I., & Head, J. W. (2008). Valley network-fed, open-basin lakes on Mars: Distribution and implications for Noachian surface and subsurface hydrology. *Icarus*, *198*(1), 37–56. https://doi.org/10.1016/j.icarus.2008.06.016

Faulk, S. P., Lora, J. M., Mitchell, J. L., & Milly, P. C. D. (2020). Titan's climate patterns and surface methane distribution due to the coupling of land hydrology and atmosphere. *Nature Astronomy*, *4*, 390–398. https://doi.org/10.1038/s41550-019-0963-0

Feng, J., Roché, M., Vigolo, D., Arnaudov, L. N., Stoyanov, S. D., Gurkov, T. D., et al. (2014). Nanoemulsions obtained via bubble-bursting at a compound interface. *Nature Physics*, *10*(8), 606–612. https://doi.org/10.1038/nphys3003

Feng, X. J., & Jiang, L. (2006). Design and creation of superwetting/antiwetting surfaces. *Advanced Materials*, *18*(23), 3063–3078. https://doi.org/10.1002/adma.200501961

Fichman, M. (2013). *Raindrop imprints and their use in the retrodeformation of carboniferous trace fossils* (Master's thesis). University of Connecticut. Retrieved from https://digitalcommons.lib.uconn.edu/

Fifer, L. M., Catling, D. C., & Toner, J. D. (2022). Chemical fractionation modeling of plumes indicates a gas-rich, moderately alkaline Enceladus ocean. *The Planetary Science Journal*, *3*(8), 191. https://doi.org/10.3847/PSJ/ac7a9f

Fritz, W. (1935). Berechnung des maximal volume von dampfblassen. *Physikalische Zeitschrift*, *36*, 379–388.

Gade, M., Hühnerfuss, H., & Korenowski, G. (2006). Marine surface films. In M. Gade, H. Hühnerfuss, & G. Korenowski (Eds.), *Chemical characteristics, influence on air-sea interactions, and remote sensing*. https://doi.org/10.1007/3-540-33271-5

Ganan-Calvo, A. M. (2022). The ocean fine spray.

Ghabache, E., Antkowiak, A., Josserand, C., & Séon, T. (2014). On the physics of fizziness: How bubble bursting controls droplets ejection. *Physics of Fluids*, *26*(12), 121701. https://doi.org/10.1063/1.4902820

Ghabache, E., & Séon, T. (2016). Size of the top jet drop produced by bubble bursting. *Physical Review Fluids*, *1*(5), 05190. https://doi.org/10.1103/physrevfluids.1.051901

Gholizadeh, M. H., Melesse, A. M., & Fuentes, H. R. (2018). Raindrop-induced erosion and sediment transport modelling in shallow waters: A review. *Journal of Soil and Water Science*, *1*, 15–25. https://doi.org/10.36959/624/427

Giraud, F. (2015). *Vaporization of water at subatmospheric pressure: Fundamentals of boiling phenomena and path towards the design of compact evaporators for sorption chillers* (Doctoral dissertation). Institut National des Sciences Appliquées de Lyon. Retrieved from https://theses.hal.science/tel-01368517

Goudge, T. A., Aureli, K. L., Head, J. W., Fassett, C. I., & Mustard, J. F. (2015). Classification and analysis of candidate impact crater-hosted closed-basin lakes on Mars. *Icarus*, *260*, 346–367. https://doi.org/10.1016/j.icarus.2015.07.026

Goudge, T. A., Head, J. W., Mustard, J. F., & Fassett, C. I. (2012). An analysis of open-basin lake deposits on Mars: Evidence for the nature of associated lacustrine deposits and post-lacustrine modification processes. *Icarus*, *219*(1), 211–229. https://doi.org/10.1016/j.icarus.2012.02.027

Grant, J. A., Wilson, S. A., Mangold, N., Calef, III, F., & Grotzinger, J. P. (2014). The timing of alluvial activity in Gale Crater, Mars. *Geophysical Research Letters*, *41*(4), 1142–1149. https://doi.org/10.1002/2013GL058909

Grasset, O., Dougherty, M. K., Coustenis, A., Bunce, E. J., Erd, C., Titov, D., et al. (2013). JUpiter ICy moons Explorer (JUICE): An ESA mission to orbit Ganymede and to characterise the Jupiter system. *Planetary and Space Science*, *78*, 1–21. https://doi.org/10.1016/j.pss.2012.12.002

Graves, S. D. B., McKay, C. P., Griffith, C. A., Ferri, F., & Fulchignoni, M. (2008). Rain and hail can reach the surface of Titan. *Planetary and Space Science*, *56*(3), 346–357. https://doi.org/10.1016/j.pss.2007.11.001

Greenberg, R. (2006). The Icy Moons of Jupiter. In P. Blondel & J. W. Mason (Eds.), *Solar system update* (pp. 197–216). Springer-Verlag. https://doi.org/10.1007/3-540-37683-6_8

Grima, C., Mastrogiuseppe, M., Hayes, A. G., Wall, S. D., Lorenz, R. D., Hofgartner, J. D., et al. (2017). Surface roughness of Titan's hydrocarbon seas. *Earth and Planetary Science Letters*, *474*, 20–24. https://doi.org/10.1016/j.epsl.2017.06.007

Grotzinger, J. P., Sumner, D. Y., Kah, L. C., Stack, K., Gupta, S., Edgar, L., et al. (2014). A habitable fluvio-lacustrine environment at Yellowknife Bay, Gale crater, Mars. *Science*, *343*(6169), 1242777. https://doi.org/10.1126/science.1242777

Hansen, C. J., Esposito, L., Stewart, A. I. F., Colwell, J., Hendrix, A., Pryor, W., et al. (2006). Enceladus' water vapor plume. *Science*, *311*(5766), 1422–1425. https://doi.org/10.1126/science.1121254
Hansen, C. J., Esposito, L. W., Colwell, J. E., Hendrix, A. R., Portyankina, G., Stewart, A. I. F., & West, R. A. (2020). The composition and structure of Enceladus' plume from the complete set of Cassini UVIS occultation observations. *Icarus*, *344*, 113461. https://doi.org/10.1016/j.icarus.2019.113461
Hapgood, K. P., Litster, J. D., Biggs, S. R., & Howes, T. (2002). Drop penetration into porous powder beds. *Journal of Colloid and Interface Science*, *253*(2), 353–366. https://doi.org/10.1006/jcis.2002.8527
Hartwig, J. W., Colozza, A., Lorenz, R. D., Oleson, S., Landis, G., Schmitz, P., et al. (2016). Exploring the depths of Kraken Mare - Power, thermal analysis, and ballast control for the Saturn Titan submarine. *Cryogenics*, *74*, 31–46. https://doi.org/10.1016/j.cryogenics.2015.09.009
Hayes, A. G., Lorenz, R. D., Donelan, M. A., Manga, M., Lunine, J. I., Schneider, T., et al. (2013). Wind driven capillary-gravity waves on Titan's lakes: Hard to detect or non-existent? *Icarus*, *225*(1), 403–412. https://doi.org/10.1016/j.icarus.2013.04.004
Hilpert, M., & Ben-David, A. (2009). Infiltration of liquid droplets into porous media: Effects of dynamic contact angle and contact angle hysteresis. *International Journal of Multiphase Flow*, *35*(3), 205–218. https://doi.org/10.1016/j.ijmultiphaseflow.2008.11.007
Hofgartner, J. D., Hayes, A. G., Lunine, J. I., Zebker, H., Lorenz, R. D., Malaska, M. J., et al. (2016). Titan's "Magic Islands": Transient features in a hydrocarbon sea. *Icarus*, *271*, 338–349. https://doi.org/10.1016/j.icarus.2016.02.022
Hofgartner, J. D., Hayes, A. G., Lunine, J. I., Zebker, H., Stiles, B. W., Sotin, C., et al. (2014). Transient features in a Titan sea. *Nature Geoscience*, *7*, 493–496. https://doi.org/10.1038/NGEO2190
Horgan, B. H. N., Anderson, R. B., Dromart, G., Amador, E. S., & Rice, M. S. (2020). The mineral diversity of Jezero crater: Evidence for possible lacustrine carbonates on Mars. *Icarus*, *339*, 113526. https://doi.org/10.1016/j.icarus.2019.113526
Hörst, S. M., & Tolbert, M. A. (2013). In situ measurements of the size and density of Titan aerosol analogs. *The Astrophysical Journal Letters*, *770*(1), L10. https://doi.org/10.1088/2041-8205/770/1/L10
Horvath, D. G., Andrews-Hanna, J. C., Newman, C. E., Mitchell, K. L., & Stiles, B. W. (2016). The influence of subsurface flow on lake formation and north polar lake distribution on Titan. *Icarus*, *277*, 103–124. https://doi.org/10.1016/j.icarus.2016.04.042
Houze, R. A., Hobbs, P. V., Herzegh, P. H., & Parsons, D. B. (1979). Size distributions of precipitation particles in frontal clouds. *Journal of Atmospheric Sciences*, *36*(1), 156–162. https://doi.org/10.1175/1520-0469(1979)036<0156:sdoppi>2.0.co;2
Howard, A. D., Moore, J. M., & Irwin, R. P. (2005). An intense terminal epoch of widespread fluvial activity on early Mars: 1. Valley network incision and associated deposits. *Journal of Geophysical Research*, *110*(E12), E12S14. https://doi.org/10.1029/2005JE002459
Howell, S. M., & Pappalardo, R. T. (2020). NASA's Europa Clipper—A mission to a potentially habitable ocean world. *Nature Communications*, *11*(1), 1311. https://doi.org/10.1038/s41467-020-15160-9
Huh, C., & Mason, S. G. (1974). The flotation of axisymmetric particles at horizontal liquid interfaces. *Journal of Colloid and Interface Science*, *47*(2), 271–289. https://doi.org/10.1016/0021-9797(74)90259-8
Hynek, B. M., Beach, M., & Hoke, M. R. T. (2010). Updated global map of Martian valley networks and implications for climate and hydrologic processes. *Journal of Geophysical Research*, *115*(E9), E09008. https://doi.org/10.1029/2009JE003548
Imanaka, H., Cruikshank, D. P., Khare, B. N., & McKay, C. P. (2012). Optical constants of Titan tholins at mid-infrared wavelengths (2.5-25 μm) and the possible chemical nature of Titan's haze particles. *Icarus*, *218*(1), 247–261. https://doi.org/10.1016/j.icarus.2011.11.018
Ingersoll, A. P., & Nakajima, M. (2016). Controlled boiling on Enceladus. 2. Model of the liquid-filled cracks. *Icarus*, *272*, 319–326. https://doi.org/10.1016/j.icarus.2015.12.040
Irwin, R. P., Craddock, R. A., Howard, A. D., & Flemming, H. L. (2011). Topographic influences on development of Martian valley networks. *Journal of Geophysical Research*, *116*(E2), E02005. https://doi.org/10.1029/2010JE003620
Ji, B., Yang, Z., & Feng, J. (2021). Compound jetting from bubble bursting at an air-oil-water interface. *Nature Communications*, *12*(1), 6305. https://doi.org/10.1038/s41467-021-26382-w
Jiang, X., Rotily, L., Villermaux, E., & Wang, X. (2022). Submicron drops from flapping bursting bubbles. *PNAS*, *119*(1), e2112924119. https://doi.org/10.1073/pnas.2112924119
Kalousova, K., & Sotin, C. (2020). The insulating effect of methane clathrate crust on Titan's thermal evolution. *Geophysical Research Letters*, *47*(13), e2020GL087481. https://doi.org/10.1029/2020GL087481
Kalová, J., & Mareš, R. (2018). The temperature dependence of the surface tension of water. *AIP Conference Proceedings*, *2047*(1), 020007. https://doi.org/10.1063/1.5081640
Katsuragi, H. (2010). Morphology scaling of drop impact onto a granular layer. *Physical Review Letters*, *104*(21), 218001. https://doi.org/10.1103/PhysRevLett.104.218001
Kazuhiro, K., Tomio, O., & Koji, E. (2017). Measurement of the maximum bubble size distribution in water subcooled flow boiling at low pressure. *International Journal of Heat and Mass Transfer*, *108*, 2365–2380. https://doi.org/10.1016/j.ijheatmasstransfer.2017.01.027
Ketcham, W. M., & Hobbs, S. G. (1969). An experimental determination of the surface energies of ice. *Philosophical Magazine A*, *19*(162), 1161–1173. https://doi.org/10.1080/14786436908228641
Kim, H.-C., & Yu, M.-J. (2005). Characterization of natural organic matter in conventional water treatment processes for selection of treatment processes focused on DBPs control. *Water Research*, *39*(19), 4779–4789. https://doi.org/10.1016/j.watres.2005.09.021
Kipping, D., Bryson, S., Burke, C., Christiansen, J., Hardegree-Ullman, K., Quarles, B., et al. (2022). An exomoon survey of 70 cool giant exoplanets and the new candidate Kepler-1708 b-i. *Nature Astronomy*, *6*(3), 367–380. https://doi.org/10.1038/s41550-021-01539-1
Knight, C. A. (1971). Experiments on the contact angle of water on ice. *Philosophical Magazine A*, *23*(181), 153–165. https://doi.org/10.1080/14786437108216369
Komen, G. J., Cavaleri, L., Donelan, M., Hasselmann, K., Hasselmann, S., & Janssen, P. A. E. M. (1994). *Dynamics and modelling of ocean waves* (1st ed.). Cambridge University Press.
Kurokawa, H., Kurosawa, K., & Usui, T. (2018). A lower limit of atmospheric pressure on early Mars inferred from nitrogen and argon isotopic compositions. *Icarus*, *299*, 443–459. https://doi.org/10.1016/j.icarus.2017.08.020
Kyzas, G. Z., & Matis, K. A. (2018). Flotation in water and wastewater treatment. *Processes*, *6*(8), 116. https://doi.org/10.3390/pr6080116
Laan, N., de Bruin, K. G., Bartolo, D., Josserand, C., & Bonn, D. (2014). Maximum diameter of impacting liquid droplets. *Physical Review Applied*, *2*(4), 044018. https://doi.org/10.1103/PhysRevApplied.2.044018
Lal, R., & Shukla, M. (2004). *Principles of soil physics*. Taylor & Francis. Retrieved from https://books.google.fr/books?id=3leGCMKvPZwC
Lamb, H. (1993). *Hydrodynamics*. Cambridge University Press.
Langhans, M. H., Jaumann, R., Stephan, K., Brown, R. H., Buratti, B. J., Clark, R. N., et al. (2012). Titan's fluvial valleys: Morphology, distribution, and spectral properties. *Planetary and Space Science*, *60*(1), 34–51. https://doi.org/10.1016/j.pss.2011.01.020
Lauro, S. E., Pettinelli, E., Caprarelli, G., Guallini, L., Rossi, A. P., Mattei, E., et al. (2021). Multiple subglacial water bodies below the south pole of Mars unveiled by new MARSIS data. *Nature Astronomy*, *5*(1), 63–70. https://doi.org/10.1038/s41550-020-1200-6

Laws, J., & Parsons, D. (1943). The relation of raindrop-size to intensity, II. *Transactions - American Geophysical Union*, *24*, 452–460.
Le Deit, L., Hauber, E., Fueten, F., Pondrelli, M., Rossi, A. P., & Jaumann, R. (2013). Sequence of infilling events in Gale Crater, Mars: Results from morphology, stratigraphy, and mineralogy. *Journal of Geophysical Research: Planets*, *118*(12), 2439–2473. https://doi.org/10.1002/2012JE004322
Lee, J. (2018). The static profile for a floating particle. *Colloids and Interfaces*, *2*(2), 18. https://doi.org/10.3390/colloids2020018
Le Gall, A., Janssen, M. A., Paillou, P., Lorenz, R. D., Wall, S. D., & the Cassini Radar Team. (2010). Radar-bright channels on Titan. *Icarus*, *207*(2), 948–958. https://doi.org/10.1016/j.icarus.2009.12.027
Leighton, T. G., & White, P. R. (2004). The Sound of Titan: A role for acoustics in space exploration. *Acoustics Bulletin*, *29*(4), 16–23. https://doi.org/10.1063/1.2354502
Le Mouélic, S., Gasnault, O., Herkenhoff, K. E., Bridges, N. T., Langevin, Y., Mangold, N., et al. (2015). The ChemCam Remote Micro-Imager at Gale crater: Review of the first year of operations on Mars. *Icarus*, *249*, 93–107. (Special Issue: First Year of MSL). https://doi.org/10.1016/j.icarus.2014.05.030
Lerman, L. (1986). Potential role of bubbles and droplets in primordial and planetary chemistry: Exploration of the liquid-gas interface as a reaction zone for condensation process. *Origins of Life and Evolution of the Biosphere*, *16*(3–4), 201–202. https://doi.org/10.1007/BF02421980
Lerman, L., & Teng, J. (2005). In the beginning – A functional first principles approach to chemical evolution. In J. Seckbach (Ed.), *Origins – Cellular origin and life in extreme habitats and astrobiology* (Vol. 6, pp. 35–55). Kuwer Academic Publisher. https://doi.org/10.1007/1-4020-2522-x_4
Lhuissier, H., & Villermaux, E. (2012). Bursting bubble aerosols. *Journal of Fluid Mechanics*, *696*, 5–44. https://doi.org/10.1017/jfm.2011.418
Liger-Belair, G., Cilindre, C., Gougeon, R., Lucioc, M., Jeandet, P., & Schmitt-Kopplin, P. (2009). Unraveling different chemical fingerprints between a champagne wine and its aerosols. *Proceedings of the National Academy of Sciences*, *106*(39), 1654–16549. https://doi.org/10.1073/pnas.0906483106
Lin, I. I., Alpers, W., & Liu, W. T. (2003). First evidence for the detection of natural surface films by the QuickSCAT scatterometer. *Geophysical Research Letters*, *30*(13), 1713. https://doi.org/10.1029/2003gl017415
Liu, J., Li, C., Zhang, R., Rao, W., Cui, X., Geng, Y., et al. (2022). Geomorphic contexts and science focus of the Zhurong landing site on Mars. *Nature Astronomy*, *6*(1), 65–71. https://doi.org/10.1038/s41550-021-01519-5
Liu, S., Liu, C. C., Froyd, K. D., Schill, G. P., Murphy, D. M., Bui, T. P., et al. (2021). Sea spray aerosol concentration modulated by sea surface temperature. *Proceedings of the National Academy of Sciences*, *118*(9), e2020583118. https://doi.org/10.1073/pnas.2020583118
Liyana-Arachchi, T. P., Zhang, Z., Ehrenhauser, F. S., Avij, P., Valsaraj, K. T., & Hung, F. R. (2014). Bubble bursting as an aerosol generation mechanism during an oil spill in the deep-sea environment: Molecular dynamics simulations of oil alkanes and dispersants in atmospheric air/salt water interfaces. *Environmental Sciences: Processes & Impacts*, *16*(1), 53–64. https://doi.org/10.1039/C3EM00391D
Loftus, K., & Wordsworth, R. D. (2021). The physics of falling raindrops in diverse planetary atmospheres. *Journal of Geophysical Research: Planets*, *126*(4), e2020JE006653. https://doi.org/10.1029/2020JE006653
Lohse, D. (2003). Bubble puzzles. *Physics Today*, *56*(2), 36–39. https://doi.org/10.1063/1.1564347
Lopes, R. M. C., Kirk, R. L., Mitchell, K. L., Legall, A., Barnes, J. W., Hayes, A., et al. (2013). Cryovolcanism on Titan: New results from Cassini RADAR and VIMS. *JGR*, *118*(3), 416–435. https://doi.org/10.1002/jgre.20062
Lora, J. M., Tokano, T., Vatant d'Ollone, J., Lebonnois, S., & Lorenz, R. D. (2019). A model intercomparison of Titan's climate and low-latitude environment. *Icarus*, *333*, 113–126. https://doi.org/10.1016/j.icarus.2019.05.031
Lorenz, R. D. (1993). The life, death and afterlife of a raindrop on Titan. *Planetary and Space Science*, *41*(9), 647–655. https://doi.org/10.1016/0032-0633(93)90048-7
Lorenz, R. D. (2022). Titan's surface bearing strength: Contact force models for the Dragonfly rotorcraft lander. *Planetary and Space Science*, *214*, 105449. https://doi.org/10.1016/j.pss.2022.105449
Lorenz, R. D., Kraal, E. R., Eddlemon, E. E., Cheney, J., & Greeley, R. (2005). Sea-surface wave growth under extraterrestrial atmospheres: Preliminary wind tunnel experiments with application to Mars and Titan. *Icarus*, *175*(2), 556–560. https://doi.org/10.1016/j.icarus.2004.11.019
Lorenz, R. D., & Lunine, J. I. (1996). Erosion on Titan: Past and present. *Icarus*, *122*(1), 79–91. https://doi.org/10.1006/icar.1996.0110
Lorenz, R. D., MacKenzie, S. M., Neish, C. D., Le Gall, A., Turtle, E. P., Barnes, J. W., et al. (2021). Selection and characteristics of the Dragonfly landing site near Selk Crater, Titan. *The Planetary Science Journal*, *2*(1), 24. https://doi.org/10.3847/psj/abd08f
Lorenz, R. D., Newman, C., & Lunine, J. I. (2010). Threshold of wave generation on Titan's lakes and seas: Effect of viscosity and implications for Cassini observations. *Icarus*, *207*(2), 932–937. https://doi.org/10.1016/j.icarus.2009.12.004
Lorenz, R. D., Turtle, E. P., Barnes, J. W., Trainer, M. G., Adams, D. S., Hibbard, K. E., et al. (2018). *Dragonfly: A Rotorcraft Lander Concept for Scientific Exploration at Titan* (Technical Report No. 3) (Vol. 34). Johns Hopkins APL.
Luspay-Kuti, A., Chevrier, V. F., Cordier, D., Rivera-Valentin, E. G., Singh, S., Wagner, A., & Wasiak, F. C. (2015). Experimental constraints on the composition and dynamics of Titan's polar lakes. *Earth and Planetary Science Letters*, *410*, 75–83. https://doi.org/10.1016/j.epsl.2014.11.023
MacIntyre, F. (1972). Flow patterns in breaking bubbles. *Journal of Geophysical Research*, *77*(27), 5211–5228. https://doi.org/10.1029/jc077i027p05211
MacKenzie, S. M., Barnes, J. W., Hofgartner, J. D., Birch, S. P. D., Hedman, M. M., Lucas, A., et al. (2019). The case for seasonal surface changes at Titan's lake district. *Nature Astronomy*, *3*(6), 506–510. https://doi.org/10.1038/s41550-018-0687-6
Malaska, M. J., Schoenfeld, A., Wynne, J. J., Mitchell, K. L., White, O., Howard, A., et al. (2022). Potential caves: Inventory of subsurface access points on the surface of Titan. *Journal of Geophysical Research: Planets*, *127*(11), e2022JE007512. https://doi.org/10.1029/2022JE007512
Malin, M. C., Ravine, M. A., Caplinger, M. A., Tony Ghaemi, F., Schaffner, J. A., Maki, J. N., et al. (2017). The Mars Science Laboratory (MSL) Mast cameras and Descent imager: Investigation and instrument descriptions. *Earth and Space Science*, *4*(8), 506–539. https://doi.org/10.1002/2016EA000252
Maltagliati, L. (2019). Ocean detection by polarization colours. *Nature Astronomy*, *3*(6), 474. https://doi.org/10.1038/s41550-019-0817-9
Mangold, N., Gupta, S., Gasnault, O., Dromart, G., Tarnas, J. D., Sholes, S. F., et al. (2021). Perseverance rover reveals an ancient delta-lake system and flood deposits at Jezero crater, Mars. *Science*, *374*(6568), 711–717. https://doi.org/10.1126/science.abl4051
Marshall, J. S., & Palmer, W. M. (1948). The distribution of raindrops with size. *Journal of Meteorology*, *5*(4), 165–166. https://doi.org/10.1175/1520-0469(1948)005<0165:tdorws>2.0.co;2
Martín-Torres, F. J., Zorzano, M.-P., Valentín-Serrano, P., Harri, A.-M., Genzer, M., Kemppinen, O., et al. (2015). Transient liquid water and water activity at Gale crater on Mars. *Nature Geoscience*, *8*(5), 357–361. https://doi.org/10.1038/ngeo2412
Mason, B. J. (1971). *The physics of clouds* (2nd ed.). Oxford University Press.
Melville, W. K. (2001). Surface, gravity and capillary waves. In J. H. Steele (Ed.), *Encyclopedia of ocean sciences* (pp. 2916–2924). Academic Press. https://doi.org/10.1006/rwos.2001.0129

Miles, J. W. (1957). On the generation of the surface waves by shear flows. *Journal of Fluid Mechanics*, *3*(02), 185–204. https://doi.org/10.1017/s0022112057000567

Mousumi, G., & Venugopal, R. (2016). Modeling of flotation process—An overview of different approaches. *Mineral Processing and Extractive Metallurgy Review*, *37*(2), 120–133. https://doi.org/10.1080/08827508.2015.1115991

Müller-Wodarg, I., Griffith, C. A., Lellouch, A., & Cravens, T. E. E. (2014). In I. Müller-Wodarg, C. A. Griffith, A. Lellouch, & T. E. Cravens (Eds.), *Titan: Interior, Surface, Atmosphere, and Space Environment*. Cambridge University Press.

Nazari-Sharabian, M., Aghababaei, M., Karakouzian, M., & Karami, M. (2020). Water on Mars—A literature review. *Galaxies*, *8*(2), 40. https://doi.org/10.3390/galaxies8020040

Neish, C. D., & Lorenz, R. D. (2012). Titan's global crater population: A new assessment. *Planetary and Space Science*, *60*(1), 26–33. https://doi.org/10.1016/j.pss.2011.02.016

Neish, C. D., Somogyi, Á., Lunine, J. I., & Smith, M. A. (2009). Low temperature hydrolysis of laboratory tholins in ammonia-water solutions: Implications for prebiotic chemistry on Titan. *Icarus*, *201*(1), 412–421. https://doi.org/10.1016/j.icarus.2009.01.003

Neish, C. D., Somogyi, Á., & Smith, M. A. (2010). Titan's primordial Soup: Formation of amino acids via low-temperature hydrolysis of tholins. *Astrobiology*, *10*(3), 337–347. https://doi.org/10.1089/ast.2009.0402

Nimmo, F., & Pappalardo, R. T. (2016). Ocean worlds in the outer solar system. *Journal of Geophysical Research: Planets*, *121*(8), 1378–1399. https://doi.org/10.1002/2016JE005081

Ojha, L., Wilhelm, M. B., Murchie, S. L., McEwen, A. S., Wray, J. J., Hanley, J., et al. (2015). Spectral evidence for hydrated salts in recurring slope lineae on Mars. *Nature Geoscience*, *8*(11), 829–832. https://doi.org/10.1038/ngeo2546

Parker, T. J., Gorsline, D. S., Saunders, R. S., Pieri, D. C., & Schneeberger, D. M. (1993). Coastal geomorphology of the Martian northern plains. *Journal of Geophysical Research*, *98*(E6), 11061–11078. https://doi.org/10.1029/93JE00618

Phillips, F. T. (1957). On the generation of waves by turbulent wind. *Journal of Fluid Mechanics*, *2*(05), 417–445. https://doi.org/10.1017/s0022112057000233

Pigott, J. S. (2011). *The viscosity of water at high pressures and high temperatures: A random walk through a subduction zone* (Master's thesis). The Ohio State University. Retrieved from http://rave.ohiolink.edu/etdc/view?acc_num=osu1299607953

Pizzo, N., Deike, L., & Ayet, A. (2021). How does the wind generate waves? *Physics Today*, *74*(11), 38–43. https://doi.org/10.1063/PT.3.4880

Porco, C. C., Helfenstein, P., Thomas, P. C., Ingersoll, A. P., Wisdom, J., West, R., et al. (2006). Cassini observes the active south pole of Enceladus. *Science*, *311*(5766), 1393–1401. https://doi.org/10.1126/science.1123013

Postberg, F., Kempf, S., Schmidt, J., Brilliantov, N., Beinsen, A., Abel, B., et al. (2009). Sodium salts in E-ring ice grains from an ocean below the surface of Enceladus. *Nature*, *459*(7250), 1098–1101. https://doi.org/10.1038/nature08046

Postberg, F., Khawaja, N., Abel, B., Choblet, G., Glein, C. R., Gudipati, M. S., et al. (2018). Macromolecular organic compound s from the depths of Enceladus. *Nature*, *558*(7711), 564–568. https://doi.org/10.1038/s41586-018-0246-4

Postberg, F., Schmidt, J., Hillier, J., Kempf, S., & Srama, R. (2011). A salt-water reservoir as the source of a compositionally stratified plume on Enceladus. *Nature*, *474*(7353), 620–622. https://doi.org/10.1038/nature10175

Ramirez, R. M., Kopparapu, R., Zugger, M. E., Robinson, T. D., Freedman, R., & Kasting, J. F. (2014). Warming early Mars with CO_2 and H_2. *Nature Geoscience*, *7*(1), 59–63. https://doi.org/10.1038/ngeo2000

Rannou, P., Curtis, D., & Tolbert, M. A. (2019). Adsorption isotherms and nucleation of methane and ethane on an analog of Titan's photochemical aerosols. *Astronomy & Astrophysics*, *631*, A151. https://doi.org/10.1051/0004-6361/201935777

Ray, B. R., & Bartell, F. E. (1953). Hysteresis of contact angle of water on paraffin. Effect of surface roughness and of purity of paraffin. *Journal of Colloid Science*, *8*(2), 214–223. https://doi.org/10.1016/0095-8522(53)90040-3

Resch, F. J., Darrozes, J. S., & Afeti, G. M. (1986). Marine liquid aerosol production from bursting of air bubbles. *Journal of Geophysical Research*, *91*(C1), 1019–1029. https://doi.org/10.1029/JC091iC01p01019

Robidel, R., Le Mouélic, S., Tobie, G., Massé, M., Seignovert, B., Sotin, C., & Rodriguez, S. (2020). Photometrically-corrected global infrared mosaics of Enceladus: New implications for its spectral diversity and geological activity. *Icarus*, *349*, 113848. https://doi.org/10.1016/j.icarus.2020.113848

Rodriguez, S., Vinatier, S., Cordier, D., Tobie, G., Achterberg, R. K., Anderson, C. M., et al. (2022). Science goals and new mission concepts for future exploration of Titan's atmosphere, geology and habitability: Titan POlar scout/orbitEr and in situ lake lander and DrONe explorer (POSEIDON). *Experimental Astronomy*, *54*(2–3), 911–973. https://doi.org/10.1007/s10686-021-09815-8

Roisman, I. V., Rioboo, R., & Tropea, C. (2002). Normal impact of a liquid drop on a dry surface: Model for spreading and receding. *Proceedings of the Royal Society A: Mathematical, Physical and Engineering Sciences*, *458*(2022), 1411–1430. https://doi.org/10.1098/rspa.2001.0923

Roth, L. (2021). A stable H_2O atmosphere on Europa's trailing hemisphere from HST images. *Geophysical Research Letters*, *48*(20), e94289. https://doi.org/10.1029/2021GL094289

Roth, L., Saur, J., Retherford, K. D., Strobel, D. F., Feldman, P. D., McGrath, M. A., & Nimmo, F. (2014). Transient water vapor at Europa's south pole. *Science*, *343*(6167), 171–174. https://doi.org/10.1126/science.1247051

Sagan, C., Thomson, W. R., & Khare, B. (1992). Titan: A laboratory for pre-biological organic chemistry. *Accounts of Chemical Research*, *25*(7), 286–292. https://doi.org/10.1021/ar00019a003

Salles, C., Poesen, J., & Covers, G. (2000). Statistical and physical analysis of soil detachment by raindrop impact: Rain erosivity indices and threshold energy. *Water Resources Research*, *36*(9), 2721–2729. https://doi.org/10.1029/2000WR900024

Scheludko, A., Toshev, B. V., & Bojadjiev, D. T. (1976). Attachment of particles to a liquid surface (capillary theory of flotation). *Journal of the Chemical Society, Faraday Transactions*, *1*(72), 2815–2828. https://doi.org/10.1039/F19767202815

Schmidt, J., Brilliantov, N., Spahn, F., & Kempf, S. (2008). Slow dust in Enceladus' plume from condensation and wall collisions in tiger stripe fractures. *Nature*, *451*(7179), 685–688. https://doi.org/10.1038/nature06491

Schmitt-Kopplin, P., Liger-Belair, G., Koch, B. P., Flerus, R., Kattner, G., Harir, M., et al. (2012). Dissolved organic matter in sea spray: A transfer study from marine surface water to aerosols. *Biogeosciences*, *9*(4), 1571–1582. https://doi.org/10.5194/bg-9-1571-2012

Schon, S. C., Head, J. W., & Fassett, C. (2012). An overfilled lacustrine system and progradational delta in Jezero crater, Mars: Implications for Noachian climate. *Planetary and Space Science*, *67*(1), 28–45. https://doi.org/10.1016/j.pss.2012.02.003

Schubert, G., Anderson, J. D., Travis, B. J., & Palguta, J. (2007). Enceladus: Present internal structure and differentiation by early and long-term radiogenic heating. *Icarus*, *188*(2), 345–355. https://doi.org/10.1016/j.icarus.2006.12.012

Schulze-Makuch, D., & Irwin, L. N. (2018). *Life in the Universe: Expectations and Constraints* (3rd ed.). Springer Nature. https://doi.org/10.1007/978-3-319-97658-7

Seignovert, B., Rannou, P., Lavvas, P., Cours, T., & West, R. A. (2017). Aerosols optical properties in Titan's detached haze layer before the equinox. *Icarus*, *292*, 13–21. https://doi.org/10.1016/j.icarus.2017.03.026

Séon, T. (2018). *Les Lois d'échelle: la physique du petit et du grand* (1st ed.). Odile Jacob.

Séon, T., & Liger-Belair, G. (2017). Effervescence in Champagne and sparkling wines: From bubble bursting to droplet evaporation. *The European Physical Journal - Special Topics*, *226*(1), 117–156. https://doi.org/10.1140/epjst/e2017-02679-6
Sephton, M. A. (2004). Meteorite composition: Organic matter in ancient meteorites. *Astronomy and Geophysics*, *45*(2), 2.08–2.14. https://doi.org/10.1046/j.1468-4004.2003.45208.x
Sephton, M. A., Verchovsky, A. B., Bland, P. A., Gilmour, I., Grady, M. M., & Wright, I. P. (2003). Investigating the variations in carbon and nitrogen isotopes in carbonaceous chondrites. *Geochimica et Cosmochimica Acta*, *67*(11), 2093–2108. https://doi.org/10.1016/S0016-7037(02)01320-0
Skotheim, T. A., Elsenbaumer, R. L., & Reynolds, J. R. (Eds.). (1998). *Handbook of conducting polymers* (2nd ed.). Marcel Dekker, Inc.
Soderblom, L. A., Kieffer, S. W., Becker, T. L., Brown, R. H., Cook, I. A. F., Hansen, C. J., et al. (1990). Triton's geyser-like plumes: Discovery and basic characterization. *Science*, *250*(4979), 410–415. https://doi.org/10.1126/science.250.4979.410
Som, S. M., Catling, D. C., Harnmeijer, J. P., Polivka, P. M., & Buick, R. (2012). Air density 2.7 billion years ago limited to less than twice modern levels by fossil raindrop imprints. *Nature*, *484*(7394), 359–362. https://doi.org/10.1038/nature10890
Sotin, C., Kalousová, K., & Tobie, G. (2021). Titan's interior structure and dynamics after the Cassini-Huygens mission. *Annual Review of Earth and Planetary Sciences*, *49*(1), 579–607. https://doi.org/10.1146/annurev-earth-072920-052847
Sparks, W. B., Schmidt, B. E., McGrath, M. A., Hand, K. P., Spencer, J. R., Cracraft, M., & E Deustua, S. (2017). Active cryovolcanism on Europa? *The Astrophysical Journal Letters*, *839*(2), L18. https://doi.org/10.3847/2041-8213/aa67f8
Stephan, K., Jaumann, R., Brown, R. H., Soderblom, J. M., Soderblom, L. A., Barnes, J. W., et al. (2010). Specular reflection on Titan: Liquids in Kraken Mare. *Geophysical Research Letters*, *37*(7), L07104. https://doi.org/10.1029/2009GL042312
Stevenson, J., Lunine, J., & Clancy, P. (2015). Membrane alternatives in worlds without oxygen: Creation of an azotosome. *Science Advances*, *1*, 1400067. https://doi.org/10.1126/sciadv.1400067
Stofan, E. R., Elachi, C., Lunine, J. I., Lorenz, R. D., Stiles, B., Mitchell, K. L., et al. (2007). The lakes of Titan. *Nature*, *445*(7123), 61–64. https://doi.org/10.1038/nature05438
Ström, G., Fredriksson, M., & Stenius, P. (1987). Contact angles, work of adhesion, and interfacial tensions at a dissolving Hydrocarbon surface. *Journal of Colloid and Interface Science*, *119*(2), 352–361. https://doi.org/10.1016/0021-9797(87)90280-3
Sun, V. Z., & Stack, K. M. (2020). Geologic map of Jezero crater and the Nili Planum region, Mars. *US Geological Survey Scientific Investigations Map*, *3464*. https://doi.org/10.3133/sim3464
Talsma, H., Van Steenbergen, M. J., Borchert, J. C. H., & Crommelin, D. J. A. (1994). A novel technique for the one-step preparation of liposomes and nonionic surfactant vesicles without the use of organic solvents. liposome formation in a continuous gas stream: The "Bubble" method. *Journal of Pharmaceutical Sciences*, *83*(3), 276–280. https://doi.org/10.1002/jps.2600830303
Trees, V. J. H., & Stam, D. M. (2019). Blue, white, and red ocean planets. Simulations of orbital variations in flux and polarization colors. *Astronomy & Astrophysics*, *626*, A129. https://doi.org/10.1051/0004-6361/201935399
Turbet, M., & Forget, F. (2021). 3-D global modelling of the early martian climate under a dense CO_2+H_2 atmosphere and for a wide range of surface water inventories. arXiv. https://doi.org/10.48550/ARXIV.2103.10301
Turtle, E. P., Perry, J. E., Barbara, J. M., Del Genio, A. D., Rodriguez, S., Le Mouélic, S., et al. (2018). Titan's meteorology over the Cassini mission: Evidence for extensive subsurface methane reservoirs. *Geophysical Research Letters*, *45*(11), 5320–5328. https://doi.org/10.1029/2018GL078170
Turtle, E. P., Perry, J. E., Hayes, A. G., Lorenz, R. D., Barnes, J. W., McEwen, A. S., et al. (2011). Rapid and extensive surface changes near Titan's equator: Evidence of April showers. *Science*, *331*(6023), 1414–1417. https://doi.org/10.1126/science.1201063
Turtle, E. P., Perry, J. E., McEwen, A. S., Del Genio, A. D., Barbara, J., West, R. A., et al. (2009). Cassini imaging of Titan's high-latitude lakes, clouds, and south-polar surface changes. *Geophysical Research Letters*, *36*(2), 2204. https://doi.org/10.1029/2008GL036186
Ulbrich, W. C. (1986). A review of the differential reflectivity technique of measuring rainfall. *IEEE Transactions on Geoscience and Remote Sensing*, *GE-24*(6), 955–965. https://doi.org/10.1109/tgrs.1986.289712
Vilella, K., Choblet, G., Tsao, W. E., & Deschamps, F. (2020). Tidally heated convection and the occurrence of melting in icy satellites: Application to Europa. *Journal of Geophysical Research: Planets*, *125*(3), e06248. https://doi.org/10.1029/2019JE006248
Villermaux, E., & Bossa, B. (2009). Size distribution of raindrops. *Nature Physics*, *6*(4), 232. https://doi.org/10.1038/nphys1648
Wagner, N. Y., Andersen, D. T., Hahn, A. S., & Johnson, S. S. (2022). Survival strategies of an anoxic microbial ecosystem in Lake Untersee, a potential analog for Enceladus. *Scientific Reports*, *12*(1), 7376. https://doi.org/10.1038/s41598-022-10876-8
Waite, J. H., Glein, C. R., Perryman, R. S., Teolis, B. D., Magee, B. A., Miller, G., et al. (2017). Cassini finds molecular hydrogen in the Enceladus plume: Evidence for hydrothermal processes. *Science*, *356*(6334), 155–159. https://doi.org/10.1126/science.aai8703
Waite, J. H., Jr., Lewis, W. S., Magee, B. A., Lunine, J. I., McKinnon, W. B., Glein, C. R., et al. (2009). Liquid water on Enceladus from observations of ammonia and ^{40}Ar in the plume. *Nature*, *460*(7254), 487–490. https://doi.org/10.1038/nature08153
Wang, X., Deane, G. B., Moore, K. A., Ryder, O. S., Stokes, M. D., Beall, C. M., et al. (2017). The role of jet and film drops in controlling the mixing state of submicron sea spray aerosol particles. *Proceedings of the National Academy of Sciences*, *114*(27), 6978–6983. https://doi.org/10.1073/pnas.1702420114
Wang, X., Ouyang, Z., Zhuo, S., Zhang, M., Zheng, G., & Wang, Y. (2014). Serpentinization, abiogenic organic compounds, and deep life. *Science China Earth Sciences*, *57*(5), 878–887. https://doi.org/10.1007/s11430-014-4821-8
Wang, Y., Yang, F., Qi, S., & Cheng, J. (2020). Estimating the effect of rain splash on soil particle transport by using a modified model: Study on short hillslopes in Northern China. *Water*, *12*(9), 2318. https://doi.org/10.3390/w12092318
Washburn, E. W. (1921). The dynamics of capillary flow. *Physical Review*, *17*(3), 273–283. https://doi.org/10.1103/PhysRev.17.273
Weislogel, M. M., Jenson, R., Chen, Y., Collicott, S. H., Klatte, J., & Dreyer, M. (2009). The capillary flow experiments aboard the International Space Station: Status. *Acta Astronautica*, *65*(5), 861–869. https://doi.org/10.1016/j.actaastro.2009.03.008
Whitford, W. G., & Duval, B. D. (2020). Chapter 4—Wind and water processes. In W. G. Whitford & B. D. Duval (Eds.), *Ecology of Desert systems* (2nd ed.), pp. 73–107). Academic Press. https://doi.org/10.1016/B978-0-12-815055-9.00004-7
Woodcock, A., Kientzler, C., Arons, A., & Blanchard, D. C. (1953). Giant condensation nuclei from bursting bubbles. *Nature*, *172*(4390), 1144–1145. https://doi.org/10.1038/1721144a0
Wu, J. (1981). Evidence of sea spray produced by bursting bubbles. *Science*, *212*(4492), 324–326. https://doi.org/10.1126/science.212.4492.324
Wu, J., Popinet, S., & Deike, L. (2022). Revisiting wind wave growth with fully coupled direct numerical simulations. *Journal of Fluid Mechanics*, *951*, A18. https://doi.org/10.1017/jfm.2022.822
Wu, X., Liu, Y., Zhang, C., Wu, Y., Zhang, F., Du, J., et al. (2021). Geological characteristics of China's Tianwen-1 landing site at Utopia Planitia, Mars. *Icarus*, *370*, 114657. https://doi.org/10.1016/j.icarus.2021.114657
Wye, L. C., Zebker, H. A., & Lorenz, R. D. (2009). Smoothness of Titan's Ontario Lacus: Constraints from Cassini RADAR specular reflection data. *Geophysical Research Letters*, *36*(16), L16201. https://doi.org/10.1029/2009GL039588

Yu, X., Hörst, S. M., He, C., McGuiggan, P., Kristiansen, K., & Zhang, X. (2020). Surface energy of the Titan aerosol analog "tholin". *The Astrophysical Journal*, *905*(2), 88. https://doi.org/10.3847/1538-4357/abc55d

Yu, X., Yu, Y., Garver, J., Zhang, X., & McGuiggan, P. (2024). The fate of simple organics on Titan's surface: A theoretical perspective. *Geophysical Research Letters*, *51*(1), e2023GL106156. https://doi.org/10.1029/2023GL106156

Zebker, H., Hayes, A., Janssen, M., Le Gall, A., Lorenz, R., & Wye, L. (2014). Surface of Ligeia Mare, Titan, from Cassini altimeter and radiometer analysis. *Geophysical Research Letters*, *41*(2), 308–313. https://doi.org/10.1002/2013GL058877

Zhao, S.-C., de Jong, R., & van der Meer, D. (2015). Raindrop impact on sand: A dynamic explanation of crater morphologies. *Soft Matter*, *11*(33), 6562–6568. https://doi.org/10.1039/C5SM00957J

Zou, C. (2013). Chapter 9 - Heavy oil and bitumen. In C. Zou (Ed.), *Unconventional petroleum geology* (pp. 307–335). Elsevier. https://doi.org/10.1016/B978-0-12-397162-3.00009-8